A fourth order Central WENO Scheme for Multi-dimensional Hyperbolic Systems of Conservation Laws

Doron Levy[†] Gabriella Puppo[‡] Giovanni Russo[§]

Abstract

We present the *first* fourth-order, central scheme for two-dimensional hyperbolic systems of conservation laws. Our new method is based on a Central Weighted Non-Oscillatory (CWENO) approach. The heart of our method is the reconstruction step, in which a genuinely two-dimensional interpolant is reconstructed from cell-averages by taking a convex combination of building blocks in the form of bi-quadratic polynomials.

Similarly to other central schemes, our new method enjoys the simplicity of the black-box approach. All that is required in order to solve a problem is to supply the flux function and an estimate on the speed of propagation. The high-resolution properties of the scheme as well as its resistance to mesh orientation, and the effectiveness of the component-wise approach, are demonstrated in a variety of numerical examples.

Key words. Hyperbolic systems, central difference schemes, high-order accuracy, non-oscillatory schemes, WENO reconstruction, CWENO reconstruction.

AMS(MOS) subject classification. 65M06.

1 Introduction

The integration of hyperbolic systems of conservation laws has initially been approached in the framework of upwind schemes, generalizing the first-order upwind Godunov scheme. Effective high-order methods based on the upwind approach are the Essentially Non-Oscillatory (ENO) schemes [7], [32] and more recently the Weighted ENO (WENO) schemes [26], [8]. For a thorough review of the schemes obtained with the upwind approach, see [31] and [6].

[†]Department of Mathematics, Stanford University, Stanford, CA 94305-2125; dlevy@math.stanford.edu

[‡]Dipartimento di Matematica, Politecnico di Torino, Corso Duca degli Abruzzi 24, 10129 Torino, Italy; puppo@calvino.polito.it

[§]Dipartimento di Matematica ed Informatica, Università di Catania, Viale Andrea Doria 6, 95125 Catania, Italy; russo@dmi.unict.it

More recently high-order central schemes have appeared. These schemes can be viewed as extensions of the first-order Lax-Friedrichs scheme [5]. They are characterized by a very simple formulation, which, unlike traditional upwind schemes, requires neither Riemann solvers (exact or approximate), nor projection of the equations along characteristic directions.

The first high-order central method obtained following these lines is the second order Nessyahu-Tadmor scheme [28]. This scheme was based on a MUSCL-type interpolant in space (see [17]), and a midpoint quadrature to approximate the time-integrals of the fluxes. For a related approach see [30]. Motivated by the simplicity and robustness of the second-order method, various high-order schemes, multi-dimensional extensions, semi-discrete schemes have been suggested in the literature, see e.g. [2, 27, 9, 10, 13, 18, 3, 19, 22, 11] and the references therein. Central schemes have been used also for hyperbolic systems with source terms. We mention here the paper [24], where a second order central scheme for systems with stiff source has been derived and applied, for example, to the systems of extended thermodynamics for a monoatomic gas, and the two papers [1, 29], where central schemes have been applied to the numerical solution of hydrodynamical models of semiconductors.

In a series of recent papers we have successfully integrated the ENO and WENO reconstruction techniques into the central framework. First, we introduced in [3], the one-dimensional Central ENO (C-ENO) scheme. The one-dimensional third and fourth-order Central WENO (CWENO) schemes were then presented in [19]. We also constructed a third-order scalar two-dimensional CWENO scheme in [21] and a third order version based on a compact stencil for 1D and 2D flows in [22]. Based on numerical evidence, it was conjectured in [20] that the one-dimensional fourth-order CWENO scheme is total-variation bounded.

The scheme we present in this paper is the *first* fourth-order, central scheme for two-dimensional hyperbolic conservation laws. The heart of our method is a new CWENO-type reconstruction in which an interpolant is being reconstructed as a convex combination of bi-quadratic polynomials.

The structure of this paper is as follows.

We start in §2 by providing a general overview on the reconstruction of two-dimensional central schemes for hyperbolic conservation laws. In particular, we explain the computation of the intermediate values required for in the prediction step, a computation which we carry out using a Natural Continuous Extension of Runge-Kutta methods.

We then proceed in §3 describing our new fourth-order CWENO-type reconstruction which is based on a fundamental bi-quadratic polynomial. First, in §3.1 we discuss the reconstruction based on cell averages. We then proceed in §3.2 by describing the analogous reconstruction based on point-values. This is required in order to obtain an accurate approximation of the integrals of the fluxes. We conclude this section in §3.4 by presenting the modifications required to adapt the scheme to systems of equations.

Finally, in §4 we present several numerical examples that test the different properties of our new scheme. We verify that the scheme is indeed fourth-order accurate. We illustrate the behavior of the weights on non-smooth solutions, study the effects of mesh orientation, real gas illustrate the robustness of the structure of the scheme under changes in the system of equations, show the effectiveness of the component-wise approach for systems of equations and end with two-dimensional Riemann problems for the gas dynamics equations.

2 Two-Dimensional Central Schemes

Consider the two-dimensional system of conservation laws

$$v_t + f(v)_x + g(v)_y = 0, \tag{2.1}$$

subject to the initial values

$$v(x, y, t{=}0) = v_0(x, y),$$

and to boundary conditions, which we do not specify at this point. The flux functions f and g are smooth vector valued functions, $f, g : \mathbb{R}^m \to \mathbb{R}^m$. The system (2.1) is assumed to be hyperbolic in the sense that for any unit vector $(n_x, n_y) \in \mathbb{R}^2$, the matrix $n_x \nabla_u f + n_y \nabla_u g$ has real eigenvalues and its eigenvectors form a basis of $\mathbb{R}^m$.

In order to integrate numerically (2.1), we introduce a rectangular grid which for simplicity will be assumed to be uniform with mesh sizes $h = \Delta x = \Delta y$ in both directions. We will denote by $I_{i,j}$ the cell centered around the grid point $(x_i, y_j) = (i\Delta x, j\Delta y)$, i.e., $I_{i,j} = [x_i - h/2, x_i + h/2] \times [y_j - h/2, y_j + h/2]$. Let Δt be the time step and denote by $w_{i,j}^n$ the point-value of a function w at the (i,j)-th grid point at time $t^n = n\Delta t$. Finally, let $\bar{w}_{i,j}^n$ denote the cell average of a function w evaluated at the point (x_i, y_j),

$$\bar{w}_{i,j}^n = \frac{1}{h^2} \int_{I_{i,j}} w(x, y, t^n)\, dx\, dy.$$

Now let u denote the numerical solution. Given the cell-averages $\{\bar{u}_{i,j}^n\}$ at time t^n, as in Godunov-type methods, central schemes provide the cell-averages at the next time-step, t^{n+1}, in the following way: first, a piecewise-polynomial reconstruction is computed from the data $\{\bar{u}_{i,j}^n\}$ resulting with

$$u^n(x, y) = \sum_{i,j} R_{i,j}(x, y) \chi_{I_{i,j}}(x, y). \tag{2.2}$$

Here, $R_{i,j}(x, y)$ is a suitable vector valued polynomial (which has to satisfy conservation, accuracy and non-oscillatory requirements), while $\chi_{I_{i,j}}(x, y)$ is the characteristic function of the cell $I_{i,j}$. Thus, in general, the function $u^n(x, y)$ will be discontinuous along the boundaries of each cell $I_{i,j}$.

In order to proceed, the reconstruction, $u^n(x, y)$, is evolved according to (2.1) for a time step Δt. In central schemes, $u^n(x, y)$ is evolved on the staggered control volume $I_{i+1/2,j+1/2} \times [t^n, t^{n+1}]$. We will use the fact that the solution remains smooth at the vertical edges of the staggered control volume, provided that the time-step Δt satisfies the CFL condition

$$\Delta t < \frac{h}{2} \frac{1}{\max(|\sigma_x|, |\sigma_y|)}.$$

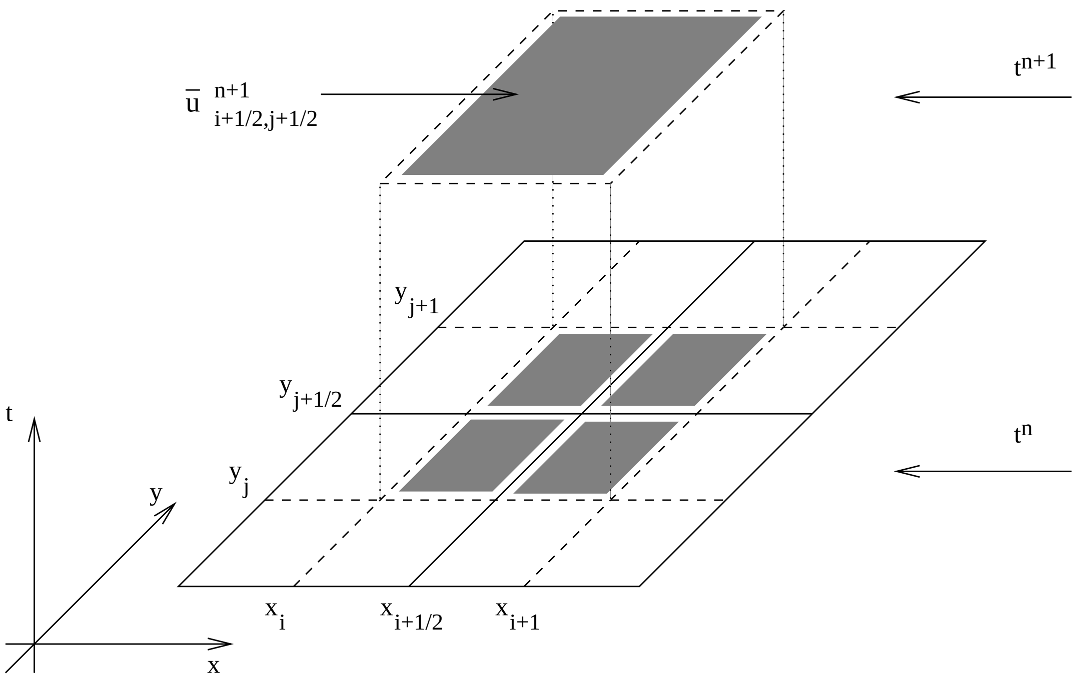

Figure 2.1: The two-dimensional stencil.

Here, $I_{i+1/2,j+1/2} = [x_i, x_{i+1}] \times [y_j, y_{j+1}]$ (see Fig. 2.1; the edges at which the solution remains smooth are denoted by dotted vertical lines), and σ_x and σ_y are the largest (in modulus) eigenvalues of the Jacobian of f and g, respectively.

An exact integration of the system (2.1) with data $u^n(x,y)$ over the control volume $I_{i+1/2,j+1/2} \times [t^n, t^{n+1}]$ results with

$$\bar{u}^{n+1}_{i+\frac{1}{2},j+\frac{1}{2}} = \frac{1}{h^2}\int\int_{I_{i+\frac{1}{2},j+\frac{1}{2}}} u^n(x,y)\, dx\, dy \tag{2.3}$$
$$- \frac{1}{h^2}\int_{\tau=t^n}^{t^{n+1}} \left\{ \int_{y=y_j}^{y_{j+1}} \left[f\left(u(x_{i+1},y,\tau)\right) - f\left(u(x_i,y,\tau)\right)\right] dy \right\} d\tau$$
$$- \frac{1}{h^2}\int_{\tau=t^n}^{t^{n+1}} \left\{ \int_{x=x_i}^{x_{i+1}} \left[g\left(u(x,y_{j+1},\tau)\right) - g\left(u(x,y_j,\tau)\right)\right] dx \right\} d\tau.$$

The first integral on the RHS of (2.3) is the cell-average of the function $u^n(x,y)$ on the staggered cell $I_{i+1/2,j+1/2}$. Given the reconstructed function $u^n(x,y)$, (2.2), this term can be computed exactly: it will consist of a contribution of four terms, resulting from averaging $R_{i+1,j+1}(x,y)$, $R_{i,j+1}(x,y)$, $R_{i+1,j}(x,y)$ and $R_{i,j}(x,y)$, on the corresponding quarter-cells.

The advantage of the central framework appears in the evaluation of the time integrals appearing in (2.3). Since the solution remains smooth on the segments $(x_i, y_j) \times [t^n, t^{n+1}]$, we can evaluate the time integrals with a quadrature rule using only nodes lying in these segments. For example, in order to obtain a fourth-order method one can use Simpson's rule for the time integrals

$$\begin{aligned}\int_{t^n}^{t^{n+1}} & f(u(x_i, y_j, z))dz = \\ &= \frac{\Delta t}{6}\left[f\left(u^n_{i,j}\right) + 4f\left(u^{n+1/2}_{i,j}\right) + f\left(u^{n+1}_{i,j}\right)\right] + O\left((\Delta t)^5\right),\end{aligned} \tag{2.4}$$

and the following centered quadrature rule in space for the integrals in space,

$$\int_{x_i}^{x_{i+1}} f(x)dx = \frac{h}{24}[-f(x_{i+2}) + 13f(x_{i+1}) + 13f(x_i) - f(x_{i-1})] + O(h^5). \tag{2.5}$$

In this way, the quadrature rule for approximating the integrals of the fluxes involves only nodes on the segments $(x_i, y_j) \times [t^n, t^{n+1}]$.

The quadrature in time, (2.4), requires the prediction of the values of the solution at later times. In the case of Simpson's rule, one has to generate the values of $u_{i,j}$ at times $t^{n+1/2}, t^{n+1}$. (The point-value $u^n_{i,j}$ can be obtained directly from the reconstruction $u_{i,j}(t^n) = u^n(x_i, y_j)$). Once again we use the smoothness of the numerical solution along the segments $(x_i, y_j) \times [t^n, t^{n+1}]$ to consider the sequence of Cauchy problems

$$\begin{cases} v'_{i,j}(z) = F(z, v_{i,j}(z)) := -f_x(v(x_i, y_j, t^n + z)) - g_y(v(x_i, y_j, t^n + z)), \\ v_{i,j}(z = 0) = u^n(x_i, y_j). \end{cases} \tag{2.6}$$

In order to obtain the mid-values at $t^{n+1/2}$ and t^{n+1}, all that is required is to solve (2.6) up to these times using a Runge-Kutta scheme. When more than one intermediate value is required (as in the case of Simpson's rule), it is possible to solve (2.6) once with the largest time required, and then reconstruct the other values with the required accuracy using the Natural Continuous Extension (NCE), [39]. More details will follow below.

Remarks:

1. The scheme which we just outlined contains no upwind differencing. This is the main advantage of the central framework. There is no need to project the system along characteristic directions. Even the evaluation of the Jacobian of the flux functions f and g is not required. We only need an estimate of the characteristic speeds to enforce a CFL-like stability condition. This makes the scheme particularly suitable for complex systems in which little information on the physical structure of the solution is available. In fact, it is very easy to adapt the scheme to a new system of equations. An illustration of this fact can be found in §4

2. A quadrature of the type (2.5) widens the stencil of the scheme while preserving the symmetry of the scheme. In principle, one can use one-sided formulas, such as,

$$\int_{x_i}^{x_{i+1}} f(x)dx = \frac{h}{12}[5f(x_i) + 8f(x_{i+1}) - f(x_{i+2})] + O(h^4),$$

or

$$\int_{x_i}^{x_{i+1}} f(x)dx = \frac{h}{12}[-f(x_{i-1}) + 8f(x_i) + 5f(x_{i+1})] + O(h^4),$$

and construct a convex combination of the two formulas, choosing the weights with a WENO-like strategy, to maximize accuracy in smooth regions (with both weights equal to 1/2 we recover (2.5)), while turning off information coming from non smooth stencils when discontinuities are detected. We have not implemented this feature because the results obtained in our tests were already satisfactory and this extra stabilization effect did not seem to be necessary.

3. In this work we do not study the issue of boundary conditions. The development of high-order, non-oscillatory schemes for boundary value problems is a difficult task that goes beyond the scope of this paper and is left for future work.

4. The motivation for the construction of a fourth order scheme, can be effectively studied in a very popular one dimensional test, see [32]. In this test a Mach 3 shock interacts with an acoustic wave. The initial condition is $u = u_L$ for $x \leq 0.1$, and $u = u_R$ for $x > 0.1$. The computational domain is $[0, 1]$, with free-flow boundary conditions. The left (L) and right (R) states are given by:

$$\begin{pmatrix} \rho \\ v \\ p \end{pmatrix}_L = \begin{pmatrix} 3.857143 \\ 2.629369 \\ 10.3333 \end{pmatrix} \qquad \begin{pmatrix} \rho \\ v \\ p \end{pmatrix}_R = \begin{pmatrix} 1 + 0.2\sin(50x) \\ 0 \\ 1 \end{pmatrix}$$

The Courant number for this flow is $c \simeq 0.219$. The solution is printed at $T = 0.18$. We show the results obtained with several central schemes in Fig. 2.2, with the same number of grid points. We note that there is a definite improvement in resolution passing from the first order Lax-Friedrichs scheme, to the second order Nessyahu-Tadmor [28] scheme, the third order Compact WENO [22] scheme, and finally the fourth order Central WENO scheme of [19], which is the one-dimensional version of the scheme proposed in this work. This test is particularly suited for illustrating the performance of a high order scheme: the presence of a rich structure behind the main shock can be resolved by the high order scheme on a relatively small number of grid points (the reference solution was obtained running the 4th order scheme on a grid with 1600 points).

2.1 The Prediction Step

For completeness, we will briefly describe the Natural Continuous Extension (NCE) of Runge-Kutta (RK) methods for obtaining the intermediate values at times $t^{n+1/2}, t^{n+1}$, by (2.6). The use of NCE permits to compute both intermediate values $u_{ij}^{n+1/2}$ and u_{ij}^{n+1} with only one RK step. This yields a considerable saving in computing time since the evaluation of the RK fluxes is the bottleneck of the time marching scheme. For more details we refer to [39] and [3].

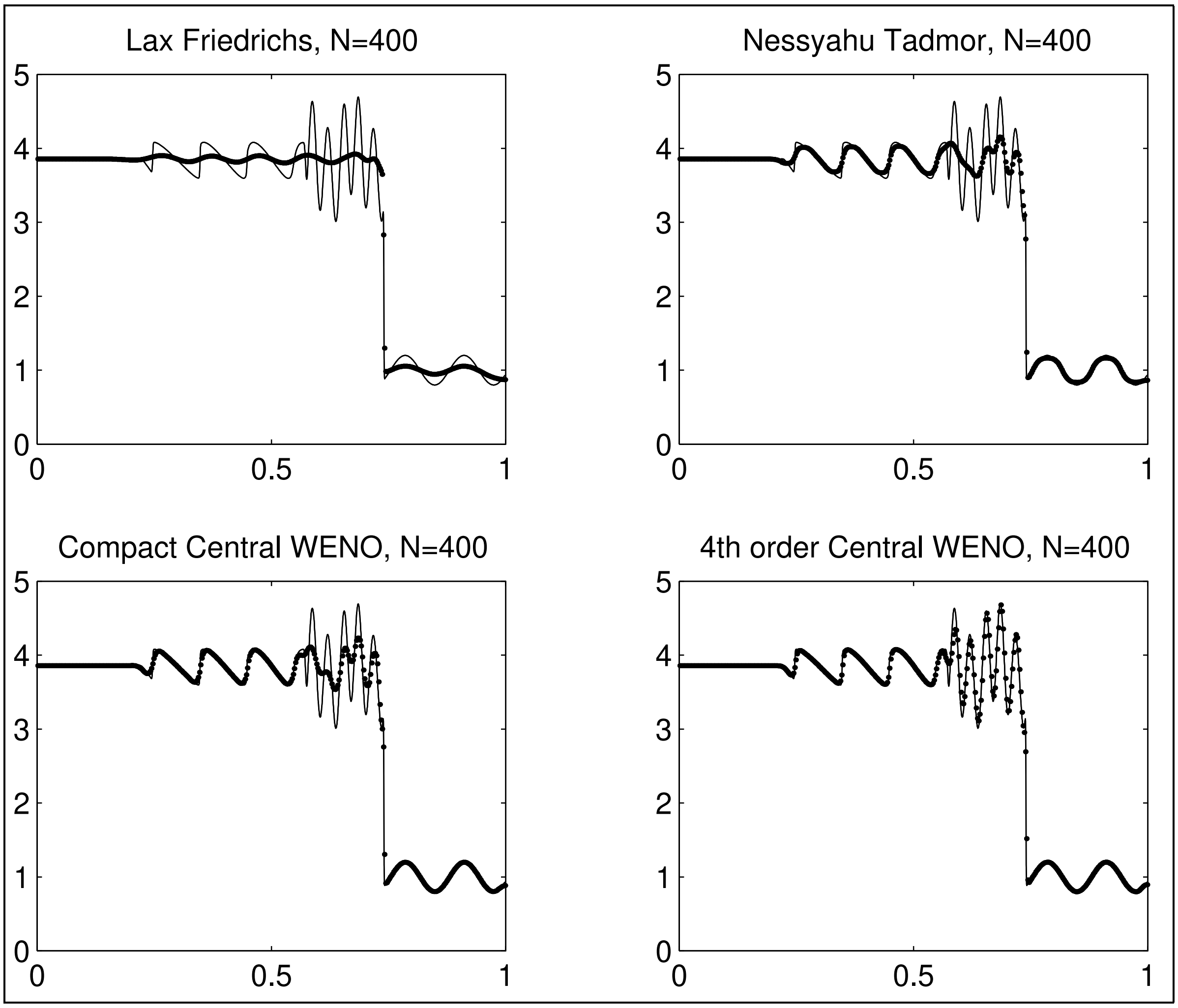

Figure 2.2: Solution of Shu-Osher acoustic-shock interaction problem at $T = 0.18$ for several central schemes.

We consider the Cauchy problem

$$\begin{cases} y' = F(t, y(t)), \\ y(t_0) = y_0. \end{cases}$$

The solution obtained at time t^{n+1} with a ν-step explicit RK scheme of order p can be written as

$$y^{n+1} = y^n + \Delta t \sum_{i=1}^{\nu} b_i K^{(i)}, \tag{2.7}$$

where the $K^{(i)}$'s are the RK fluxes

$$K^{(i)} = F\left(t^n + \Delta t\, c_i, y_n + \Delta t \sum_{j=1}^{i-1} a_{ij} K^{(j)}\right), \qquad c_i = \sum_{j=1}^{i} a_{ij}. \tag{2.8}$$

We can combine the data y^n, y^{n+1}, and the RK fluxes, $K^{(i)}$, to obtain an extension of the numerical solution of the ODE, namely, there exist ν polynomials $b_i(\theta)$ of degree $d \leq p$, such that

1. $y(t^n + \theta\Delta t) = y^n + \Delta t \sum_{i=1}^{\nu} b_i(\theta) K^{(i)}, \qquad 0 \leq \theta \leq 1,$
2. $y(t^n) = y^n, \quad y(t^n + \Delta t) = y^{n+1},$
3. $\max_{0\leq\theta\leq 1} |y^{(l)}(t^n + \theta\Delta t) - w^{(l)}(t^n + \theta\Delta t)| = O(\Delta t^{d+1-l}),$

where $w(t)$ is the exact solution of the ODE at time t^n. For a uniformly fourth-order accurate scheme in time, we need $d+1=4$, i.e., $d=3$. ¿From the theory of NCE it follows that in order to obtain fourth-order accurate values, it is necessary to use a fourth-order RK scheme (in fact no third-order RK scheme has a $d=3$ extension).

The NCE of a fourth-order RK scheme is:

$$\begin{aligned} b_1(\theta) &= 2(1-4b_1)\theta^3 + 3(3b_1 - 1)\theta^2 + \theta \\ b_i(\theta) &= 4(3c_i - 2)b_i\theta^3 + 3(3-4c_i)b_i\theta^2, \qquad i = 2,3,4. \end{aligned}$$

The standard fourth-order RK method we use reads

$$b = \begin{pmatrix} 1/6 \\ 1/3 \\ 1/3 \\ 1/6 \end{pmatrix}, \qquad a = \begin{pmatrix} 0 & 0 & 0 & 0 \\ 1/2 & 0 & 0 & 0 \\ 0 & 1/2 & 0 & 0 \\ 0 & 0 & 1 & 0 \end{pmatrix}, \qquad c = \begin{pmatrix} 0 \\ 1/2 \\ 1/2 \\ 1 \end{pmatrix}.$$

Since we need to predict the values of the solution at time $t^{n+1/2}$ and t^{n+1}, we have

$$\begin{aligned} y\left(t^n + \frac{\Delta t}{2}\right) &= y^n + \Delta t \sum_{i=1}^{4} b_i\left(\frac{1}{2}\right) K^{(i)} = y^n + \frac{\Delta t}{6}\left(\frac{5}{4}K^1 + K^2 + K^3 - \frac{1}{4}K^4\right), \\ y\left(t^n + \Delta t\right) &= y^n + \Delta t \sum_{i=1}^{4} b_i(1) K^{(i)} = y^n + \frac{\Delta t}{6}\left(K^1 + 2K^2 + 2K^3 + K^4\right). \end{aligned}$$

Remark: The prediction step, (2.6), requires a non-oscillatory evaluation of the point-values of the derivatives of the fluxes, $f_x(u)$ and $g_y(u)$, at the grid points (x_i, y_j). This issue will be addressed below.

3 The Reconstruction Step

In this section we will describe in detail our new reconstruction step. We start with the reconstruction from cell-averages, (2.2), which is needed at the beginning of each time-step. We then proceed with the reconstruction from point-values which is used for evaluating the fluxes in the ODE (2.6). This section ends with a discussion of the modifications to the algorithm which are required for solving systems of equations.

3.1 The Reconstruction from Cell Averages

In every cell $I_{i,j}$ we reconstruct a bi-quadratic polynomial, $R_{i,j}(x,y)$, which is written as a convex combination of nine bi-quadratic polynomials, $P_{i,j}(x,y)$, centered in the cells around $I_{i,j}$,

$$R_{i,j}(x,y) = \sum_{l,k=-1}^{1} w_{i,j}^{l,k} P_{i+l,j+k}(x,y). \tag{3.1}$$

The bi-quadratic polynomials $P_{i,j}(x,y)$, which serve as the building blocks for the reconstruction (3.1), interpolate the data $\{\bar{u}^n\}$ in the sense of cell averages (see below). They approximate the function $u(x,y)$ whose cell averages are $\{\bar{u}^n\}$ with third order accuracy. The combination (3.1) is designed to increase accuracy *and* to prevent spurious oscillations. The weights $w_{i,j}^{l,k}$ in (3.1) are computed using a nonlinear algorithm which must satisfy the stability requirement, $w_{i,j}^{l,k} \geq 0$, and a conservation requirement, $\sum_{l,k=-1}^{1} w_{i,j}^{l,k} = 1$.

For simplicity of notation, let us introduce the 3×3 matrices:

$$(\Omega_{i,j})_{l,k} = w_{i,j}^{l,k}, \qquad l,k = -1,0,1.$$

Thus each matrix $\Omega_{i,j}$ contains the nine non-constant weights needed to compute the reconstruction on the cell $I_{i,j}$. Note that the first index, l, is associated with the x-variable, while the index k is associated with the y-variable.

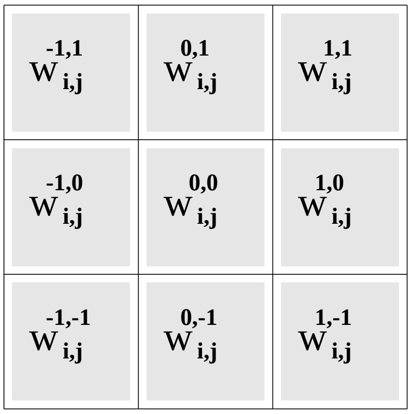

Figure 3.1: The weight matrix $\Omega_{i,j}$.

Let $I_{i,j}^m$, $m = 1,\ldots,4$, denote the four quarters of the cell $I_{i,j}$, with $I_{i,j}^1$ being the upper-right quarter while the other three quarters are numbered clock-wise (see Fig. 3.2). In order to obtain a fourth-order computation of the first term on the RHS of (2.3), the reconstructed polynomial, $R_{i,j}(x,y)$, must recover the averages over the four quarter cells with fourth-order accuracy,

$$\bar{R}_{i,j}^{(m)} := \frac{4}{h^2}\int_{I_{i,j}^m} R_{i,j}(x,y,t^n)dxdy = \frac{4}{h^2}\int_{I_{i,j}^m} u(x,y,t^n) + O(h^4), \quad m = 1,\ldots,4, \tag{3.2}$$

where $u(x, y, t^n)$ denotes the exact solution of the equation at time t^n. On the other hand, the derivatives of the fluxes should be recovered with third-order accuracy. In this case, cancellation occurs, so that one order of accuracy is gained on smooth flows. We therefore need to accurately evaluate the intermediate values, $u(x, y, t^n + C_i\Delta t)$, with $C_1 = 1/2$ and $C_2 = 1$, (see (2.7)), and in particular, we need an accurate reconstruction of the point-values of the solution at the integer grid points (i, j) at time t^n.

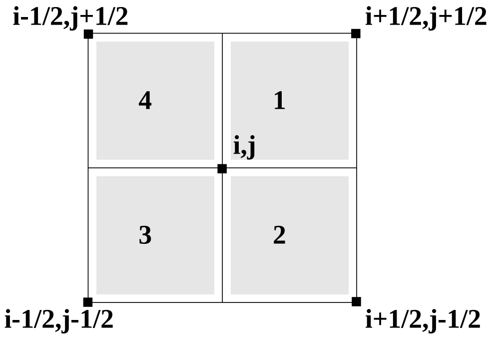

Figure 3.2: The quarter cells.

The output of the reconstruction routine from cell averages at the beginning of the time step must therefore provide a fourth-order approximation of

(a) the four quarter-cell averages

$$\bar{R}^{(m)}_{i,j} = \frac{4}{h^2} \sum_{l,k=-1}^{1} w^{l,k}_{i,j} \int_{I^m_{i,j}} P_{i+l,j+k}(x, y)\, dxdy, \qquad m = 1, \ldots, 4. \tag{3.3}$$

(b) the point-values at the integer grid-points

$$R_{i,j}(x_i, y_j) = \sum_{l,k=-1}^{1} w^{l,k}_{i,j} P_{i+l,j+k}(x_i, y_j). \tag{3.4}$$

The reconstruction routine from point values called at each evaluation of the Runge-Kutta fluxes must provide a third order approximation of the derivatives of the flux at the integer grid points

$$R^x_{i,j}(x_i, y_j) = \sum_{l,k=-1}^{1} w^{l,k}_{i,j} \partial_x P_{i+l,j+k}(x_i, y_j), \tag{3.5}$$

$$R^y_{i,j}(x_i, y_j) = \sum_{l,k=-1}^{1} w^{l,k}_{i,j} \partial_y P_{i+l,j+k}(x_i, y_j), \tag{3.6}$$

where the polynomials $P_{i+l,j+k}$ interpolate the data $f(u(\cdot, \cdot))$ in (3.5), while in (3.6) the polynomials $P_{i+l,j+k}$ interpolate the data $g(u(\cdot, \cdot))$. Generally, the weights $w^{l,k}_{i,j}$ in (3.3) and in (3.4) will be different from the weights in (3.5) and (3.6) due to the different accuracy requirements.

We would like to stress that there is no need to explicitly compute all the coefficients of the polynomial $R_{i,j}(x,y)$. All that is needed are the point-values and the quarter-cell averages of these polynomials, or their derivatives at the grid points.

We are now ready to present the construction of the fundamental bi-quadratic polynomials, $P_{i,j}(x,y)$.

3.1.1 The Bi-Quadratic Polynomials

In this section we explicitly give the coefficients of the interpolating polynomials $P_{i,j}(x,y)$, which serve as the building block for the reconstruction of $R_{i,j}(x,y)$ in (3.1). In each cell, $I_{i,j}$, we write the polynomial $P_{i,j}(x,y)$ as

$$\begin{aligned} P_{i,j}(x,y) \;=\; & b_0 + b_1(x-x_i) + b_2(y-y_j) + b_3(x-x_i)(y-y_j) + \\ & + b_4(x-x_i)^2 + b_5(y-y_j)^2 + b_6(x-x_i)^2(y-y_j) + \\ & + b_7(x-x_i)(y-y_j)^2 + b_8(x-x_i)^2(y-y_j)^2, \end{aligned} \tag{3.7}$$

where for simplicity we have omitted the indices (i,j) from the coefficients $\{b_m\}$. The nine coefficients b_m are uniquely determined by the interpolation conditions

$$\frac{1}{h^2}\int_{x_i-\frac{h}{2}+lh}^{x_i+\frac{h}{2}+lh}\int_{y_j-\frac{h}{2}+kh}^{y_j+\frac{h}{2}+kh} P_{i,j}(x,y)dydx = \bar{u}_{i+l,j+k}, \qquad l,k=-1,0,1,$$

i.e., the polynomials $P_{i,j}(x,y)$ interpolate the data $\{\bar{u}_{i,j}\}$ in the sense of cell-averages. The resulting expressions of the coefficients are

$$\begin{aligned} & b_0 = \bar{u} - \tfrac{h^2}{24}(\hat{u}_{xx}+\hat{u}_{yy}) + \tfrac{h^4}{24^2}\hat{u}_{xxyy}, && b_1 = \hat{u}_x - \tfrac{h^2}{24}\hat{u}_{xyy}, \\ & b_2 = \hat{u}_y - \tfrac{h^2}{24}\hat{u}_{xxy}, && b_3 = \hat{u}_{xy}, \\ & b_4 = \tfrac{1}{2}\hat{u}_{xx} - \tfrac{h^2}{48}\hat{u}_{xxyy}, && b_5 = \tfrac{1}{2}\hat{u}_{yy} - \tfrac{h^2}{48}\hat{u}_{xxyy}, \\ & b_6 = \tfrac{1}{2}\hat{u}_{xxy}, && b_7 = \tfrac{1}{2}\hat{u}_{xyy}, \\ & b_8 = \tfrac{1}{4}\hat{u}_{xxyy}, \end{aligned}$$

where the following notation for divided differences was used,

$$\begin{aligned} \hat{u}_{x_{i,j}} &= \frac{\bar{u}_{i+1,j}-\bar{u}_{i-1,j}}{2h}, \qquad \hat{u}_{y_{i,j}} = \frac{\bar{u}_{i,j+1}-\bar{u}_{i,j-1}}{2h}, \\ \hat{u}_{xx_{i,j}} &= \frac{\bar{u}_{i+1,j}-2\bar{u}_{i,j}+\bar{u}_{i-1,j}}{h^2}, \qquad \hat{u}_{yy_{i,j}} = \frac{\bar{u}_{i,j+1}-2\bar{u}_{i,j}+\bar{u}_{i,j-1}}{h^2}, \\ \hat{u}_{xy_{i,j}} &= \frac{\bar{u}_{i+1,j+1}-\bar{u}_{i+1,j-1}-\bar{u}_{i-1,j+1}+\bar{u}_{i-1,j-1}}{4h^2}, \\ \hat{u}_{xyy_{i,j}} &= \frac{(\bar{u}_{i+1,j+1}-2\bar{u}_{i+1,j}+\bar{u}_{i+1,j-1})-(\bar{u}_{i-1,j+1}-2\bar{u}_{i-1,j}+\bar{u}_{i-1,j-1})}{2h^3}, \end{aligned}$$

$$
\begin{aligned}
\hat{u}_{xxy_{i,j}} &= \frac{(\bar{u}_{i+1,j+1} - 2\bar{u}_{i,j+1} + \bar{u}_{i-1,j+1}) - (\bar{u}_{i+1,j-1} - 2\bar{u}_{i,j-1} + \bar{u}_{i-1,j-1})}{2h^3}, \\
\hat{u}_{xxyy_{i,j}} &= \frac{1}{h^4}\Big[(\bar{u}_{i+1,j+1} - 2\bar{u}_{i+1,j} + \bar{u}_{i+1,j-1}) - 2(\bar{u}_{i,j+1} - 2\bar{u}_{i,j} + \bar{u}_{i,j-1}) + \\
&\quad +(\bar{u}_{i-1,j+1} - 2\bar{u}_{i-1,j} + \bar{u}_{i-1,j-1})\Big].
\end{aligned}
$$

Remark: We would like to emphasize that the reconstruction $R_{i,j}(x,y)$ is conservative,

$$
\frac{1}{h^2}\int_{I_{i,j}} R_{i,j}(x,y)dxdy = \frac{1}{h^2}\sum_{l,k} w_{i,j}^{l,k}\int_{I_{i,j}} P_{i+l,j+k}(x,y)dxdy = \frac{1}{h^2}\sum_{l,k} w_{i,j}^{l,k} h^2 \bar{u}_{i,j} = \bar{u}_{i,j}.
$$

The second equality holds because of the interpolation requirements on the $P_{i,j}$'s and the third equality holds because the weights $w_{i,j}^{l,k}$ must add up to one.

3.1.2 The Weights

The weights $w_{i,j}^{l,k}$ in the reconstruction (3.1) are computed following the WENO/CWENO ideas presented in [26], [8] and [19]. The goal is to choose weights such that

(a) In smooth regions maximum accuracy is obtained.

(b) In non-smooth regions, information coming from non-smooth stencils should be switched off in order to prevent the onset of spurious oscillations.

In order to achieve these goals, the weights $w_{i,j}^{l,k}$ are written as

$$
w_{i,j}^{l,k} = \frac{\alpha_{i,j}^{l,k}}{\sum_{l,k=-1}^{1} \alpha_{i,j}^{l,k}}, \tag{3.8}
$$

where

$$
\alpha_{i,j}^{l,k} = \frac{C^{l,k}}{(\epsilon + S_{i,j}^{l,k})^p}. \tag{3.9}
$$

Here, $C^{l,k}$ are the constants which are chosen in order to maximize accuracy in smooth regions, $S_{i,j}^{l,k}$ are the "smoothness indicators" (see below), p is a constant and ϵ is introduced in order to prevent division by zero. Following our previous works (e.g. [19]), in all our numerical experiments we use $p = 2$ and $\epsilon = 10^{-6}$.

The "smoothness indicators", $S_{i,j}^{l,k}$, are designed to measure the smoothness of the polynomials $P_{i+l,j+k}$ in the cell $I_{i,j}$. This is done by evaluating a suitable function of the norms of the derivatives of the polynomial on the cell $I_{i,j}$, namely

$$
S_{i,j}^{l,k} = \int_{I_{i,j}} \left(|\partial_x P_{i+l,j+k}|^2 + |\partial_y P_{i+l,j+k}|^2 + h^2|\partial_{xx}^2 P_{i+l,j+k}|^2 + h^2|\partial_{yy}^2 P_{i+l,j+k}|^2\right)\, dx\, dy. \tag{3.10}
$$

The integrals in (3.10) can be computed exactly, but they involve a large number of function evaluations. In this work, the integrals were evaluated with a Gaussian quadrature with four nodes on the rectangle $I_{i,j}$.

All is left is to compute the constants $C^{l,k}$ in (3.9).

We seek the values of a set of constants, $C^{l,k}$, such that the integral of the reconstruction on each quarter-cell is fourth-order accurate.

We start with the upper-right quarter cell and use symmetry considerations to label $C^{l,k}$ as $q_1, \dots q_6$, such that, $C^{1,1} = q_1$, $C^{1,0} = C^{0,1} = q_2$, $C^{-1,1} = C^{1,-1} = q_3$, $C^{-1,0} = C^{0,-1} = q_4$, $C^{-1,-1} = q_5$ and $C^{0,0} = q_6$, (see Fig. 3.3). Since $C^{l,k} \geq 0$ and $\sum_{l,k=-1}^{1} C^{l,k} = 1$, we have

$$q_6 = 1 - q_1 - 2q_2 - 2q_3 - 2q_4 - q_5, \qquad q_m \geq 0.$$

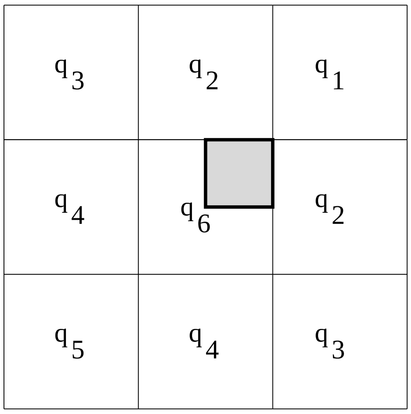

Figure 3.3: The nine weights.

Imposing the accuracy requirements (3.2) for the upper-right quarter cell, results with the following system

$$\begin{cases} q_2 = -q_1 + q_4 + q_5, \\ \\ q_3 = \frac{3}{16} - q_4 - q_5, \end{cases}$$

while q_1, q_4 and q_5 remain arbitrary. One can use this freedom to set as many as possible $q_m = 0$. This would make the scheme more efficient but less robust since it will cancel out possible stencils whose information might be desirable. We have preferred to select all the q_m's to be different from zero so that each stencil can be present in the reconstruction.

One possibility is to choose $q_1 = q_4 = q_5 = \frac{1}{16}$, from which it follows that $q_2 = q_3 = \frac{1}{16}$ and $q_6 = \frac{1}{2}$. This gives a symmetric combination which can be therefore used for all four quarter-cell averages (and not only for the upper-right quarter cell),

$$\mathbb{C} = \begin{pmatrix} 1/16 & 1/16 & 1/16 \\ 1/16 & 1/2 & 1/16 \\ 1/16 & 1/16 & 1/16 \end{pmatrix}. \tag{3.11}$$

By symmetry, this specific choice of $\mathbb{C}$ also gives fourth-order accuracy for the computation of point-values at the center of the cell.

Finally, we would like to comment that in principle one could compute the smoothness indicators in every step of the RK method. In our numerical examples we compute them only once at the beginning of each time-step.

3.2 The Reconstruction of Flux Derivatives

In order to compute each RK flux in (2.6), it is necessary to evaluate the function

$$F(u)_{i,j} := -f_x(u) - g_y(u)\Big|_{i,j}, \tag{3.12}$$

where u is evaluated at each intermediate time $t_i = t^n + \Delta t\, c_i$ of the RK scheme, (2.7). It is therefore necessary to compute the intermediate values of u:

$$u_{i,j}^{(l)} = u_{i,j}^n + \Delta t \sum_{k=1}^{l-1} a_{l,k} K^{(k)}, \tag{3.13}$$

where the Runge-Kutta fluxes K^k's were defined in (2.8). Given the intermediate values in (3.13) we can evaluate $f(u_{i,j}^{(l)})$ and $g(u_{i,j}^{(l)})$, which can be then used to compute the discrete derivatives of f and g required in (3.12). These derivatives can be calculated using a procedure which is equivalent to the reconstruction procedure that was used earlier. This time, however, we require that the point-values of the derivative of the reconstruction will be third-order accurate. For simplicity, assume that we start with the function $u_{i,j}$. As before, we write the final reconstruction as a convex combination of interpolating polynomials (compare with (3.1)),

$$R_{i,j}(x,y) = \sum_{l,k=-1}^{1} \tilde{w}_{i,j}^{l,k} \tilde{P}_{i+l,j+k}(x,y). \tag{3.14}$$

This time, the polynomials interpolate the data in the sense of point-values

$$\tilde{P}_{i,j}(x_{i+l}, y_{j+k}) = \tilde{u}_{i+l,j+k} \quad l,k = -1,0,1.$$

where $\tilde{u}_{i+l,j+k}$ denotes either $f(u_{i+l,j+k})$ or $g(u_{i+l,j+k})$.

The non-constant coefficients in (3.14) are (compare with (3.8)),

$$\tilde{w}_{i,j}^{l,k} = \frac{\tilde{\alpha}_{i,j}^{l,k}}{\sum_{l,k=-1}^{1} \tilde{\alpha}_{i,j}^{l,k}},$$

where for the derivative in the x-direction, one has

$$\tilde{\alpha}_{i,j}^{l,k} = \frac{\tilde{C}_x^{l,k}}{(\epsilon + S_{i,j}^{l,k})^p},$$

and a similar expression holds for the derivative in the y-direction. The smoothness indicators are the same as those computed at the beginning of the time-step. Since we are interested in an accurate reconstruction of the derivatives in (3.12), the constants $\tilde{C}_x^{l,k}$ must be chosen in order to satisfy

$$|\partial_x R_{i,j} - u_x(x_i, y_j)| = O(h^3).$$

A straightforward computation results with the possible choice of $\tilde{C}_x^{l,k}$ as

$$\tilde{C}_x^{l,k} = \begin{pmatrix} 0 & 0 & 0 \\ 1/6 & 2/3 & 1/6 \\ 0 & 0 & 0 \end{pmatrix}. \tag{3.15}$$

For the y-derivative one can choose the transpose of (3.15), $\tilde{C}_y^{l,k} = (\tilde{C}_x^{l,k})^t$. With this choice, the mixed terms of the bi-quadratic polynomials do not play any role and the differentiation formulas become very simple:

$$\begin{aligned} \left.\frac{\partial R_{i,j}}{\partial x}\right|_{(x_i,y_j)} &= \sum_{l=-1}^{1} \tilde{w}_{i,j}^{l,0} \left.\frac{\partial \tilde{P}_{i+l,j}}{\partial x}\right|_{(x_i,y_j)} \\ \left.\frac{\partial R_{i,j}}{\partial y}\right|_{(x_i,y_j)} &= \sum_{k=-1}^{1} \tilde{w}_{i,j}^{0,k} \left.\frac{\partial \tilde{P}_{i,j+k}}{\partial x}\right|_{(x_i,y_j)} \end{aligned} \tag{3.16}$$

3.3 The Algorithm

We would like to summarize the different stages of the algorithm obtained in the previous sections. Given $\bar{u}_{i,j}^n$, compute $\bar{u}_{i+1/2,j+1/2,}^{n+1}$ according to (2.3), i.e.,

$$\bar{u}_{i+1/2,j+1/2}^{n+1} = \mathcal{I}_1 + \mathcal{I}_2,$$

where

$$\mathcal{I}_1 = \frac{1}{h^2} \int\int_{I_{i+\frac{1}{2},j+\frac{1}{2}}} u^n(x,y)\, dx\, dy,$$

and

$$\begin{aligned} \mathcal{I}_2 = & - \frac{1}{h^2} \int_{\tau=t^n}^{t^{n+1}} \left\{ \int_{y=y_j}^{y_{j+1}} \left[f\left(u(x_{i+1},y,\tau)\right) - f\left(u(x_i,y,\tau)\right)\right] dy \right\} d\tau \\ & - \frac{1}{h^2} \int_{\tau=t^n}^{t^{n+1}} \left\{ \int_{x=x_i}^{x_{i+1}} \left[g\left(u(x,y_{j+1},\tau)\right) - g\left(u(x,y_j,\tau)\right)\right] dx \right\} d\tau. \end{aligned}$$

$\mathcal{I}_1$ is the sum of the four quarter-cell averages defined in (3.3),

$$\mathcal{I}_1 = \bar{R}_{i,j}^{(1)} + \bar{R}_{i,j+1}^{(2)} + \bar{R}_{i+1,j+1}^{(3)} + \bar{R}_{i+1,j}^{(4)}$$

where the polynomials $P_{i+l,j+k}(x,y)$ appearing in (3.3) are given by (3.7) and the weights $w_{i,j}^{l,k}$ are given by (3.8).

The integrals in $\mathcal{I}_2$ are replaced by the quadrature (2.4) and (2.5).

$$\begin{aligned} &\int_{t^n}^{t^{n+1}} f(u(x_i,y_j,z))dz = \\ &\quad = \frac{\Delta t}{6}\left[f\left(u_{i,j}^n\right) + 4f\left(u_{i,j}^{n+1/2}\right) + f\left(u_{i,j}^{n+1}\right)\right] + O\left((\Delta t)^5\right), \end{aligned}$$

and

$$\int_{x_i}^{x_{i+1}} f(x)dx = \frac{h}{24}[-f(x_{i+2}) + 13f(x_{i+1}) + 13f(x_i) - f(x_{i-1})] + O(h^5).$$

The time quadrature required the prediction of the mid-values, which can be obtained with the RK scheme, (2.7). This ODE solver requires on the RHS the values of the derivatives of the fluxes given by (3.16), which are evaluated at the integer grid-points (and therefore utilizes the point-values recovered by (3.4)).

3.4 Systems of Equations

There are not that many modifications required in order to solve systems of equations instead of solving scalar equations. Basically, one has to extend the algorithm to systems using a straightforward component-wise approach.

The only delicate point is the computation of the smoothness indicators. A component-wise evolution of the smoothness indicators where each component may relay on a different stencil has some disadvantages, as already pointed out in [19]. We also showed in [19] that the simplest and most robust way to compute the smoothness indicators is to apply *global smoothness indicators*: all components have the same indicator, which is computed as an average of the smoothness indicators of each component,

$$S_{i,j}^{l,k} = \frac{1}{d}\sum_{m=1}^{d}\left\{\int_{I_{i,j}}\left(|\partial_x P^m_{i+l,j+k}|^2 + |\partial_y P^m_{i+l,j+k}|^2 + h^2|\partial^2_{xx}P^m_{i+l,j+k}|^2 + \right.\right. \tag{3.17}$$
$$\left.\left. + h^2|\partial^2_{yy}P^m_{i+l,j+k}|^2\right)dxdy\right\}\left(\|\bar{u}^{(m)}\|_2 + \epsilon\right)^{-1}.$$

Here $P^m_{i,j}$ denotes the m-th component of the vector valued interpolation polynomial, centered on the cell $I_{i,j}$, and:

$$\|\bar{u}^{(m)}\|_2^2 = \sum_{i,j}|\bar{u}^{(m)}_{i,j}|^2\,h^2,$$

where (m) denotes the m-th component of the vector $\bar{u}_{i,j}$. Therefore, the Global Smoothness Indicator is an average of all componentwise Smoothness Indicators, each of which is normalized with respect to the norm of the corresponding field.

4 Numerical Examples

The numerical tests we include are designed to investigate the following points:

1. Evaluate the **accuracy** of the scheme.
2. Illustrate the **behavior of the weights** on non smooth solutions.
3. Show the **non-oscillatory properties** of the scheme on non-smooth solutions.
4. Study the **effect of mesh orientation** with respect to wave fronts on the numerical solution.
5. Show the effectiveness of the **black box approach** in the ability to deal with different systems of equations, with only minor modifications in the code.
6. Show the effectiveness of the **component-wise approach** in a test problem where the components of the solution have jumps located at different positions. This test reveals whether a discontinuity in one of the components induces spurious oscillations in a different component.

7. Show the behavior of the scheme in **gas dynamics** test problems resulting in flows with a complex structure.

We wish to observe that we chose our test problems in order to illustrate the behavior of the scheme by itself.

We avoided some of the classical test problems of gas dynamics (as those in [38]) because the solution in those problems depends very strongly on an accurate discretization of boundary conditions. Since at present it is still not known how to implement non-oscillatory high-order accurate boundary conditions, we preferred test problems for which a conflict with boundary conditions could be prevented.

4.1 Accuracy Tests

We start with the accuracy tests by considering the initial data

$$u_0(x,y) = \sin^2(\pi x)\sin^2(\pi y)$$

with periodic boundary conditions on the square $[0,1]\times[0,1]$. We solve a two-dimensional linear advection equation with the fluxes taken as $f(u) = g(u) = u$. The solution is sampled after one complete cycle ($T = 1$). The mesh ratio is $\lambda = \Delta t/h = 0.45$. We compute the error in the discrete L^∞ and L^1 norms, defined respectively as:

$$\begin{aligned} ||u||_\infty &= \max_{i,j} |u_{i,j}|, \\ ||u||_1 &= \textstyle\sum_{i,j} |u_{i,j}|\, h^2. \end{aligned}$$

We first compute the accuracy using constant weights in the reconstruction. These weights are given by equation (3.11). The results are shown in Table 4.1 and are verified to be fourth-order order accurate both in the L^∞ and in the L^1 norms.

In Table 4.2 we show the results obtained with the fully nonlinear scheme, with the weights defined in (3.8) and (3.9). Once again, we observe the fourth-order accuracy of the scheme. Moreover, even for very coarse grids, the errors obtained with the nonlinear weights are comparable to the errors resulting from the linear scheme, which is the scheme that maximizes accuracy on smooth solutions.

Linear advection, Constant weights

N	L^1 error	L^1 order	L^∞ error	L^∞ order
10	6.687E-03	-	1.646E-02	-
20	4.562E-04	3.87	1.106E-03	3.90
40	2.905E-05	3.97	6.811E-05	4.02
80	1.812E-06	4.00	4.197E-06	4.02
160	1.133E-07	4.00	2.601E-07	4.01

Table 4.1: $T = 1$, $\lambda = 0.45$, $u_0(x) = \sin^2(\pi x)\sin^2(\pi y)$.

Linear advection, Nonlinear weights

N	L^1 error	L^1 order	L^∞ error	L^∞ order
10	8.763E-03	-	2.464E-02	-
20	5.092E-04	4.10	1.632E-03	3.92
40	3.001E-05	4.08	8.747E-05	4.22
80	1.828E-06	4.04	4.836E-06	4.18
160	1.135E-07	4.01	2.802E-07	4.11

Table 4.2: $T = 1$, $\lambda = 0.45$, $u_0(x) = \sin^2(\pi x)\sin^2(\pi y)$.

4.2 The Nonlinear Weights

We consider an initial square patch

$$u_0(x,y) = \begin{cases} 1, & |x-\frac{1}{2}| < \frac{1}{2} \quad \text{and} \quad |y-\frac{1}{2}| < \frac{1}{2}, \\ 0, & \text{otherwise,} \end{cases}$$

on the square $[0,1] \times [0,1]$. We rotate the patch with a linear flow yielding a constant angular velocity, namely:

$$f(u,x,y) = -\left(y-\frac{1}{2}\right)\frac{\pi}{2}u, \quad g(u,x,y) = \left(x-\frac{1}{2}\right)\frac{\pi}{2}u.$$

Figure 4.1 shows the solution at $T = .5$ and $T = 1$ together with corresponding plots of the central weight. It is clear that the central weight drops almost to zero where the central stencil contains non-smooth regions. On the other hand, the central weight is larger than its equilibrium value 1/2 in the middle of the transition regions, where the central stencil carries smooth information, while some of the one sided stencils could contribute oscillations. Where the solution is smooth, the central weight is close to its optimal value, 1/2. The number of grid points in each direction is $N = 40$, while $\lambda = 0.425$.

4.3 Non-oscillatory Properties

We have already seen in Fig. 4.1 that the numerical solution of the linear rotation problem has no spurious oscillations. We now consider the initial condition taken from [9]:

0.8	0.5
-1	-0.2

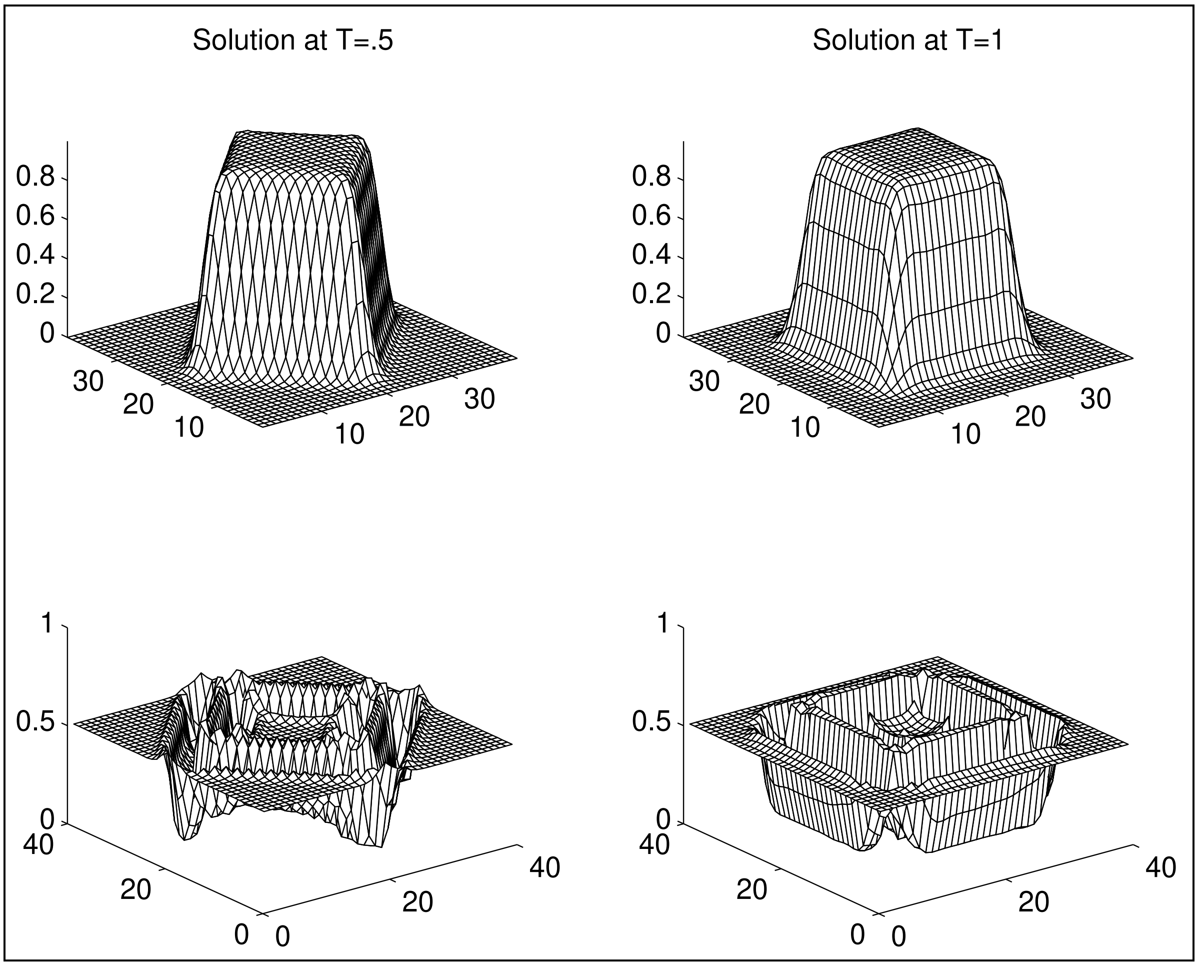

Figure 4.1: Linear rotation. Solution and central weight at $T = .5$ and $T = 1$. $N = 40$, $\lambda = .425$.

The configuration is centered at $(1/2, 1/2)$, and the computational region is $[0,1] \times [0,1]$. The boundary conditions are $\partial u/\partial n = 0$. Such conditions are perfectly justified until the signal reaches the boundary. The flux is Burgers', $f(u) = g(u) = -u^2/2$. The number of grid points in each direction is $N = 80$, and $\lambda = .25$.

The solution at $T = .5$ is shown in Fig. 4.2. The figure shows the control of spurious oscillations in a problem involving shock interaction. There are some small amplitude wiggles, which are better visible in the contour plot on the right of the figure, but the features of the solution are well resolved. The present scheme in fact implements ENO-like ideas: the presence of spurious oscillations is possible, especially close to the interaction of discontinuities, where the scheme does not degenerate to first order accuracy. However such wiggles have small amplitude. All discontinuities are very sharp. This can be compared to the resolution of discontinuities in Fig. 4.1. In the latter case all discontinuities are contacts: with no artificial compression these discontinuities are naturally less resolved than shock waves.

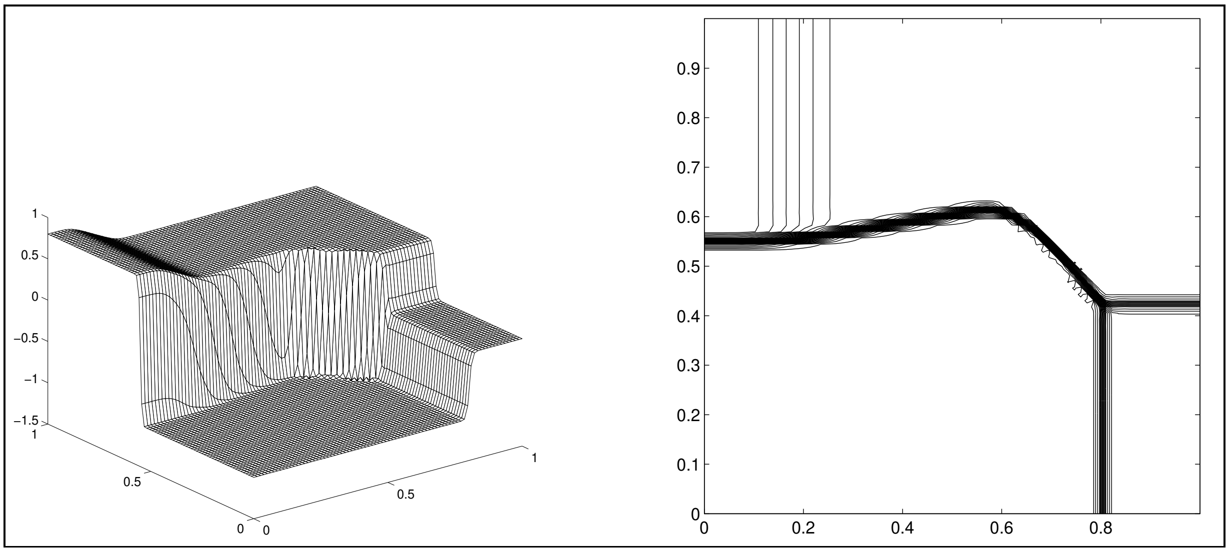

Figure 4.2: Burgers equation. Solution at $T = .5$. $N = 80$, $\lambda = .25$. The contour plot has 21 level lines.

4.4 Mesh Orientation

A common problem encountered when working with rectangular grids is that the solution has a natural bias in the directions of the coordinates. In our case, we find a very weak dependence of the solution on the mesh orientation. Moreover, this bias improves dramatically under mesh refinement. We first show a test in which an initial step, making an angle θ with the x-direction, is linearly advected. The initial condition is

$$\overline{u}_0(x, y) = \arctan\left[s\left(x - \frac{1}{\tan(\theta)}\left(y - \frac{1-h}{2}\right) - \frac{1}{2}\right)\right],$$

with $s = 1000$. The flux is linear, with $f(u) = g(u) = -u$, and boundary conditions are imposed in order to ensure that the flow is constant on lines parallel to the wave front. In Fig. 4.3 we show the results obtained with a 40×40 grid, with $\lambda = 0.25$, for several values of θ.

It is apparent from the figure that there are no spurious oscillations, regardless of the orientation of the wave front with respect to the grid. Moreover, the resolution seems to be the same in all directions considered. In other words, it seems that, in this case, the orientation of the grid has no effect on the numerical solution.

We also show a nonlinear test. Fig. 4.4 shows the numerical solution computed on a two-dimensional gas dynamics problem. Here a one-dimensional shock-tube initial value problem is considered, with the initial discontinuity making an angle $\theta = 60°$ with the x axis. The 2D gas dynamics equations are specified in the next section. The initial data for the shock tube problem are the classical ones proposed by Sod [35]:

$$\begin{pmatrix}\rho\\ u\\ p\end{pmatrix}_L = \begin{pmatrix}1\\ 0\\ 1\end{pmatrix}, \qquad \begin{pmatrix}\rho\\ u\\ p\end{pmatrix}_R = \begin{pmatrix}0.125\\ 0\\ 0.1\end{pmatrix}.$$

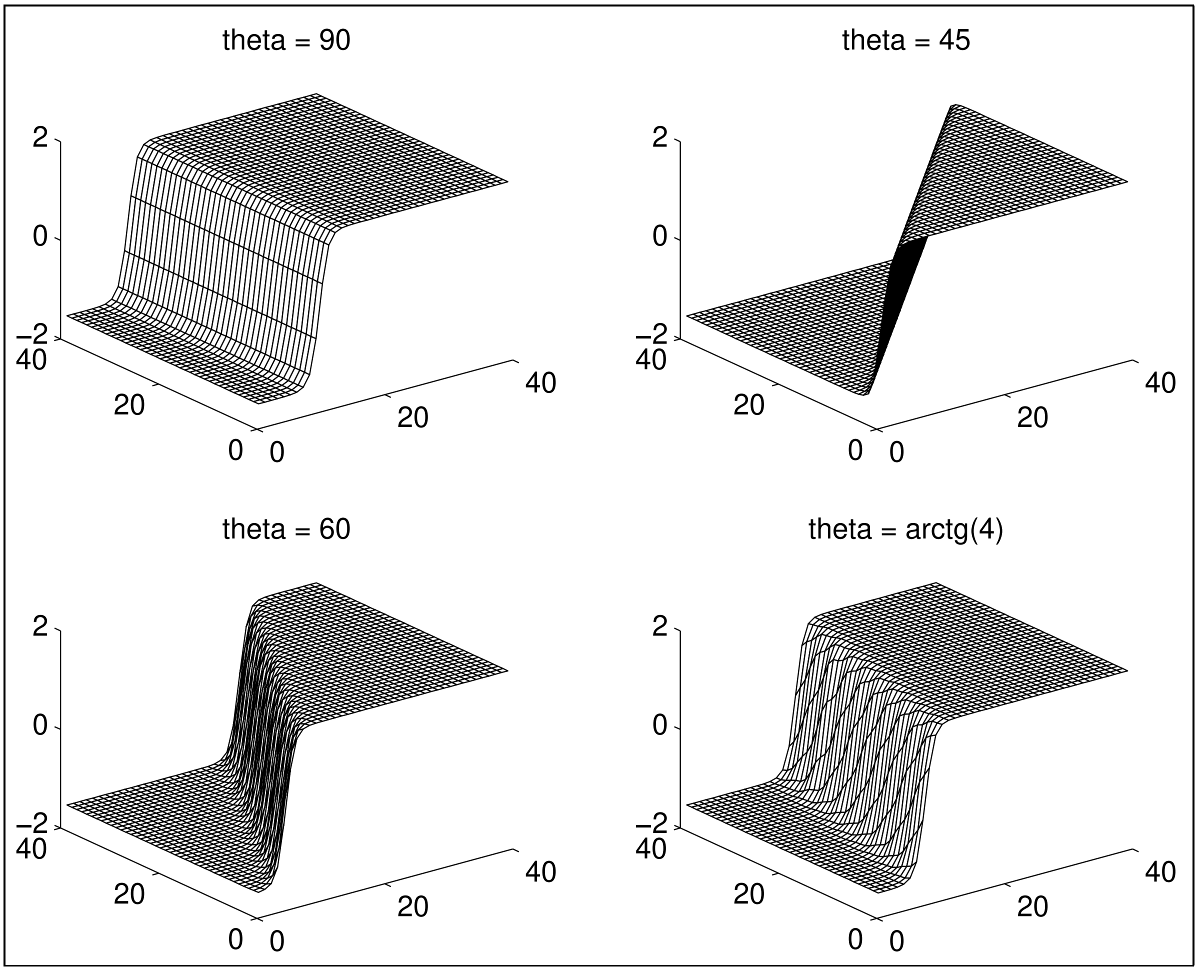

Figure 4.3: Linear advection of a step skew to the grid. $N = 40$, $\lambda = 0.25$.

The computational region is the rectangle $[0, 1] \times [0, 0.25]$, with 200 points in the x direction and 50 points in the y direction. The solution is sampled at $y = 0.125$ at $T = 0.1386$ and compared with the exact one dimensional solution at $T = 0.16 = 0.1386/\sin(\theta)$ (left of Fig. 4.4). The right side of the figure shows the contour plot of the 2D solution. Clearly, the flow is still perfectly one-dimensional, i.e. no perturbations deriving from the grid orientation are apparent. There are a few small amplitude wiggles, around the contact discontinuity. This phenomenon was already present in the one dimensional case, [19].

Finally, we show the results obtained on a problem with radial symmetry. Following [23], we consider a shock tube initial condition with radial symmetry, namely:

$$u(x, y, t = 0) = \begin{cases} u_L & (x - 0.5)^2 + (y - 0.5)^2 \le R^2 \\ u_R & \text{otherwise,} \end{cases}$$

with $R = 0.2$ and where u_L and u_R are again the left and right states respectively of Sod's shock tube problem. The computational region is $[0, 1]^2$. The results in $T = 0.1$ appear in Fig. 4.5, for $N = 100$ and $N = 200$ grid points in each direction.

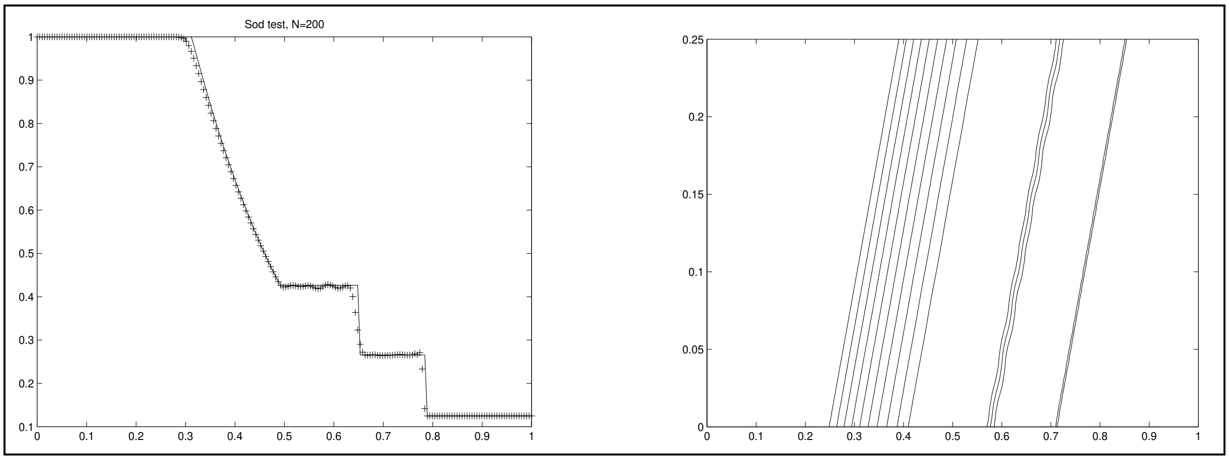

Figure 4.4: Oblique Sod's shock tube problem, $\theta = \pi/3$ Comparison with the exact solution and contour plot. The grid is 200×50. $\lambda = .2$

The scatter plots appearing at the top of Fig. 4.5 are computed re-writing the solution $u(x, y)$ as a function of $r = \sqrt{(x-0.5)^2 + (y-0.5)^2}$. Several profiles are obtained in this fashion. Here they have all been superposed. If the solution had perfect radial symmetry, all profiles would lie on the same curve. Thus the thickness of the curve one obtains gives a measure of the lack of symmetry of the solution. In Fig. 4.5, we note that the solution obtained with the C-WENO scheme does not have perfect radial symmetry. We note however that the results improve dramatically under grid refinement: on the right of Fig. 4.5 approximately 200 profiles are superposed, while only approximately 100 are superposed on the left. However, the thickness of the curve is now reduced. Moreover it is important to note that the main features of the flow (i.e. the wave fronts and tails) have an almost perfect radial symmetry, as can be readily seen in the contour plots at the bottom of Fig. 4.5. The deviations from symmetry concern only the fluctuations around the states between the main wave fronts.

These results would probably improve modifying the quadrature rule for the fluxes, as suggested in [23]. It is noteworthy to note that the results we obtain with the 4th order scheme seem to have a better resolution than those shown in [23], which were obtained with the second order Nessyahu-Tadmor scheme.

4.5 Black-Box Approach

We now consider the Euler equations with the Van der Waals equation of state (EOS) for a real gas. The purpose of this section is to show that the scheme is able to deal with different problems, with very few changes in the code. The EOS we are considering is:

$$p(\rho, e) = (\gamma - 1)\frac{\rho e + a\rho^2}{1 - \rho b} - a\rho^2. \tag{4.1}$$

Upwind schemes based on Riemann solvers require in depth modifications to deal with a change in the equation of state. Even upwind schemes based on projection along

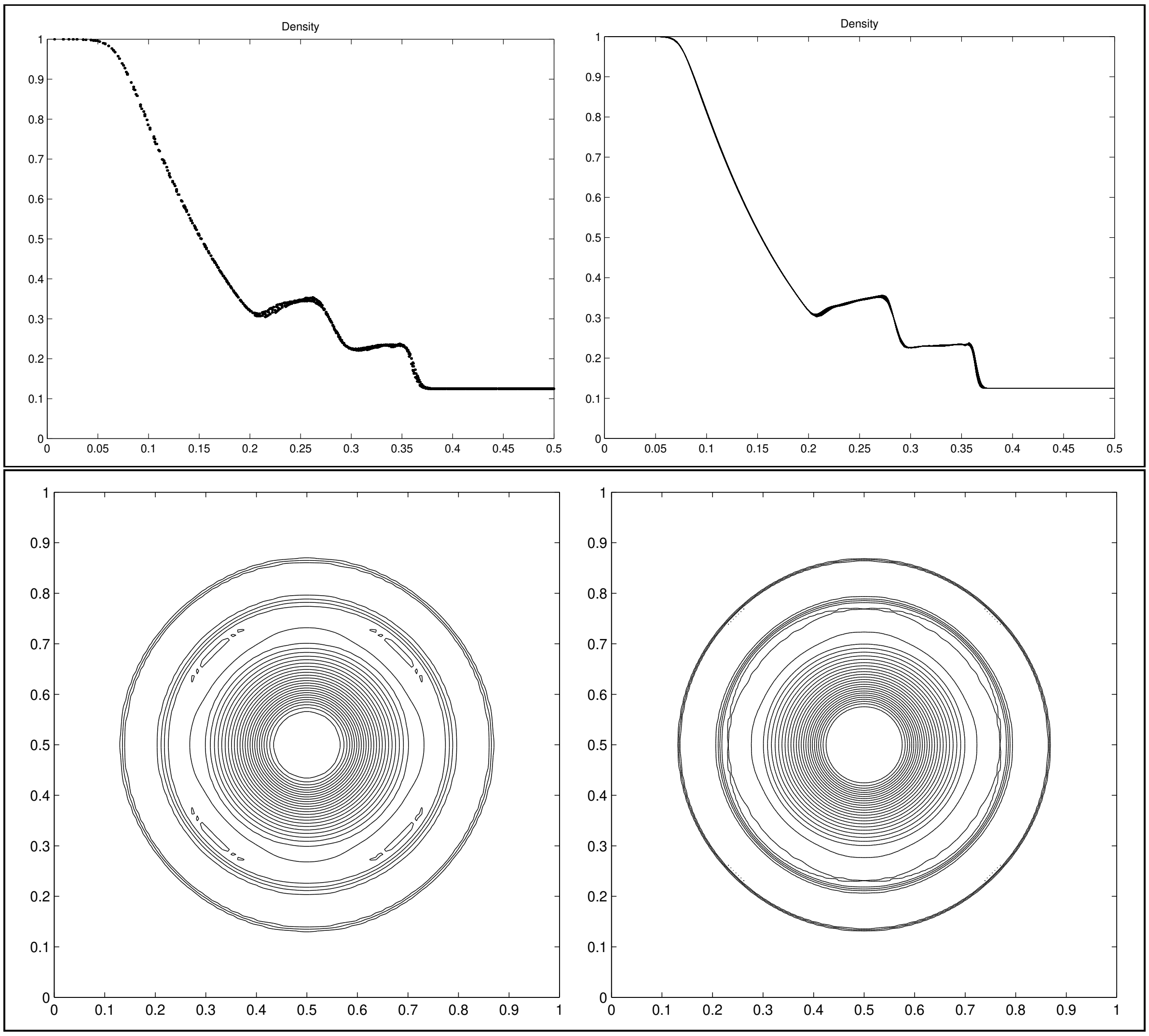

Figure 4.5: Solution with circular symmetry. Scatter plots (top) and contour plots (bottom) for the density, for $N = 100$ (left) and $N = 200$ (right) grid points, $\lambda = 0.2$. The contour plots have 30 equally spaced contour lines.

characteristic directions require a considerable amount of extra work to deal with such a simple change, see for instance [36]. Here we only need to change *one* line in the function that computes the fluxes. Namely, we just need to update the instruction that computes the pressure, starting from the conserved variables.

To illustrate this fact, we run our scheme on the oblique shock tube problem, we have described in the previous subsection, with Sod's initial data, on a Van der Waals gas. As in [36], we pick $\gamma = 1.4$, $a = 0.03412$ and $b = 0.23$ for the parameters appearing in (4.1). We compute the solution up to $T = 0.1386$, with $\lambda = 0.2$ and $N = 200$.

Our results are shown in Fig. 4.6. The left of the figure shows a comparison with the solution obtained in the ideal gas case. We note that the two solutions are similar, as expected, and have an analogous pattern of small amplitude spurious wiggles: i.e. the

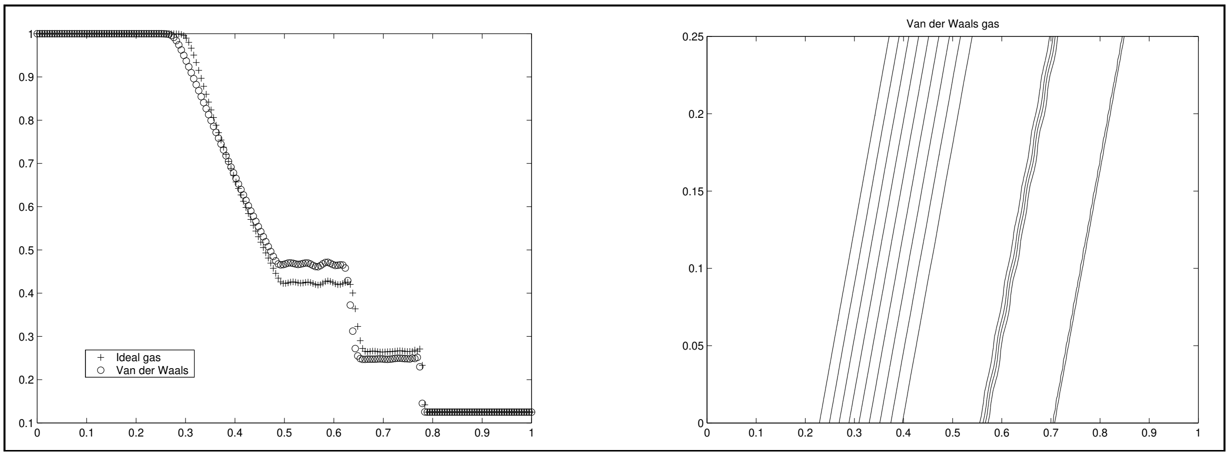

Figure 4.6: Oblique Sod's shock tube problem, with Van der Waals gas, $\theta = \pi/3$ Comparison with the ideal gas solution and contour plot. The grid is 200×50. $\lambda = .2$

numerical solution has not worsened with the change in the EOS. The resolution is also approximately the same. The right of the figure shows a contour plot: as in the ideal gas case, no mesh orientation effect is visible.

The results shown in [36] on the same test problem with a second and a third order scheme show no spurious oscillations. Again, it is not surprising that an ad-hoc scheme can exhibit better results on a specific problem than those obtained with our multi-purpose scheme. However, it is noteworthy that the resolution in the results, published in [36] with the third order scheme, seems to be comparable with ours. Actually, the resolution of the CWENO scheme might be even better: the CWENO solution in fact resolves the contact discontinuity in roughly 3 grid points at $T = 0.1386$, while the third order upwind scheme in [36] resolves the contact discontinuity in 3 grid points at $T = 0.09$.

4.6 Component-wise Approach

The test shown here has been discussed in [9] as a one dimensional test. The test consists of a 2×2 linear system, with initial conditions chosen in order to yield a contact discontinuity in each of the characteristic fields, traveling at different speeds.

The one dimensional system we consider is

$$u_t + Au_x = 0, \qquad A = \begin{pmatrix} 0 & 1 \\ 1 & 0 \end{pmatrix},$$

subject to the initial conditions

$$u_1(x,0) \equiv 0, \qquad u_2(x,0) = \begin{cases} 1 & x < 1/2 \\ 0 & x > 1/2 \end{cases}.$$

The corresponding 2D system has been chosen as:

$$u_t + Au_x + Bu_y = 0, \qquad A = \begin{pmatrix} 0 & 1 \\ 1 & 0 \end{pmatrix}, \qquad B = -\cot\theta \begin{pmatrix} 0 & 1 \\ 1 & 0 \end{pmatrix},$$

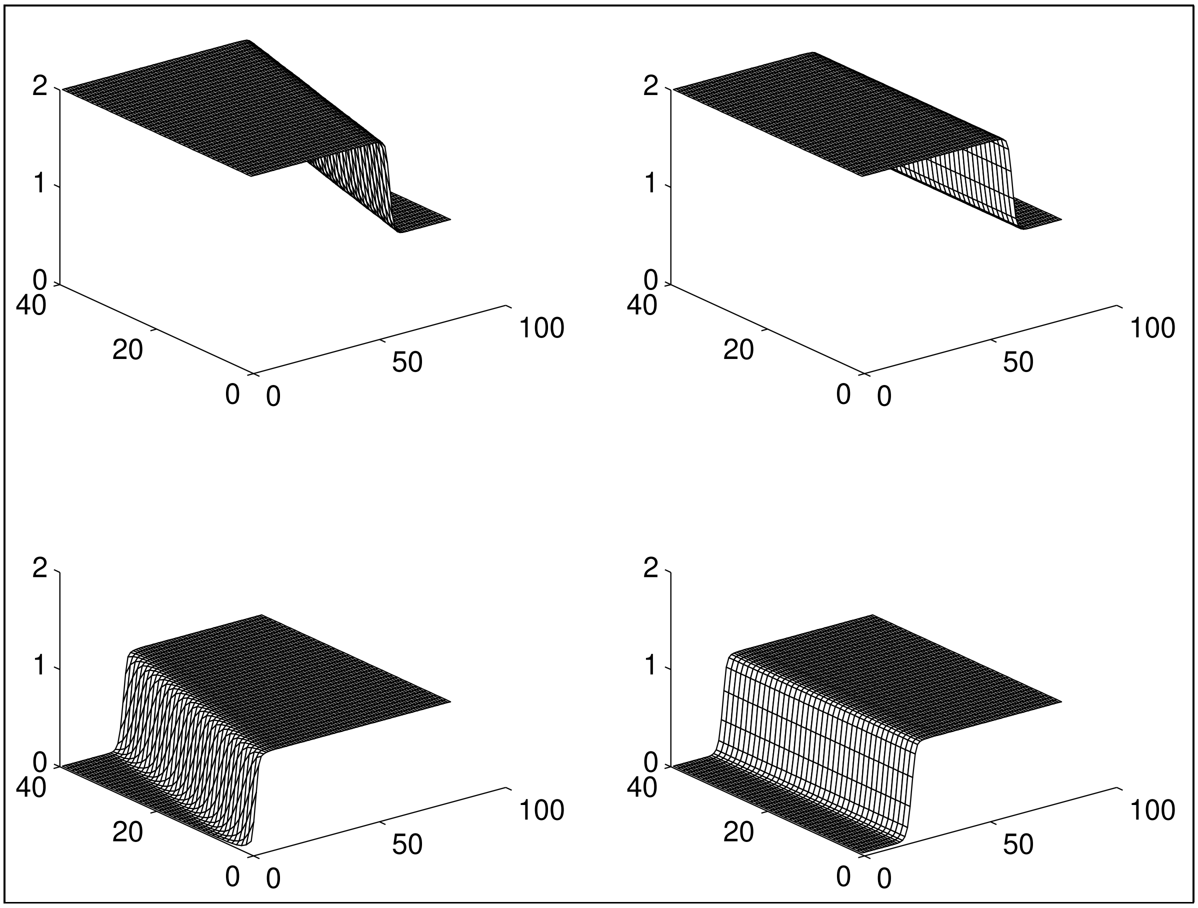

Figure 4.7: Linear advection of a step skew to the grid; 2×2 system. Characteristic variables: $v_1 = u_1 + u_2$ and $v_2 = u_1 - u_2$. On the left $\theta = \pi/3$, on the right $\theta = \pi/2$. The grid is 100×40. $\lambda = .25$

with initial conditions:

$$u_1(x_i, y_j, t = 0) \equiv 0, \qquad u_2(x_i, y_j, t = 0) = \begin{cases} 1 & x_i < (y_j - 1/2)\cot\theta \\ 0 & \text{otherwise} \end{cases}.$$

A purely component-wise approach may result in spurious oscillations in each characteristic variable, located where the other characteristic field undergoes a discontinuity.

Our results are shown in Fig. 4.7. The solution is shown in a 2D setting, in which the initial discontinuity makes an angle $\theta = 60°$ (left column) and $\theta = 90°$ (second column) with the x axis. The two rows show the two characteristic variables, $v_1 = u_1 + u_2$ and $v_2 = u_1 - u_2$. Again, no spurious oscillations are observed.

4.7 Two-Dimensional Gas Dynamics Equations

We consider the system of equations for gas dynamics in 2D

$$U_t + F(U)_x + G(U)_y = 0,$$

$\begin{pmatrix} \rho \\ u \\ v \\ p \end{pmatrix} = \begin{pmatrix} 2 \\ -0.75 \\ 0.5 \\ 1 \end{pmatrix}$	$\begin{pmatrix} \rho \\ u \\ v \\ p \end{pmatrix} = \begin{pmatrix} 1 \\ -0.75 \\ -0.5 \\ 1 \end{pmatrix}$
$\begin{pmatrix} \rho \\ u \\ v \\ p \end{pmatrix} = \begin{pmatrix} 1 \\ 0.75 \\ 0.5 \\ 1 \end{pmatrix}$	$\begin{pmatrix} \rho \\ u \\ v \\ p \end{pmatrix} = \begin{pmatrix} 3 \\ 0.75 \\ -0.5 \\ 1 \end{pmatrix}$

Figure 4.8: Initial condition for configuration 5.

where

$$U = \begin{pmatrix} \rho \\ \rho u \\ \rho v \\ E \end{pmatrix}, \qquad F(U) = \begin{pmatrix} \rho u \\ \rho u^2 + p \\ \rho uv \\ u(E+p) \end{pmatrix}, \qquad G(U) = \begin{pmatrix} \rho v \\ \rho uv \\ \rho v^2 + p \\ v(E+p) \end{pmatrix}.$$

Here, ρ is the density, u and v are the two components of the velocity, $E = \rho e + \frac{1}{2}\rho(u^2+v^2)$ is the total energy per unit volume, and e is the internal energy of the gas. The system is closed by defining the pressure p through the equation of state. For a perfect gas $p = \rho e(\gamma - 1)$, where the constant γ is the ratio of specific heats. In all tests considered, $\gamma = 1.4$.

For a study of Riemann problems for the two-dimensional gas dynamics equations we refer the reader to [33, 34]. A numerical study based on a characteristic approach was performed by Lax and Liu in [16]. A more recent work in which a second-order semi-discrete central scheme was used for the study of similar problems was presented by Kurganov and Tadmor in [14].

The test problems shown below are two dimensional Riemann problems. We compare our results with those shown in [16]. In particular, following the notation introduced in [16], we will show the results obtained for Configuration 5 and Configuration 16. Configuration 5 corresponds to the initial condition shown in Fig. 4.8. These initial data result in four interacting contact discontinuities.

The results are shown in Fig. 4.9 at time T=0.23. On the left we show the density obtained with a 200×200 grid, while on the right we show the density on a 400×400 grid. The time step is one half the one chosen in [16], due to our more restrictive CFL, namely $\lambda = 0.5 * 0.2494$.

We first note that there is a very strong increase in resolution as the cell dimensions are halved due to the high-order accuracy of the scheme. When we compare the results obtained on the fine grid with the corresponding ones in Fig. 5 of [16], we find that the two pictures are of comparable resolution. Although the positive schemes used by

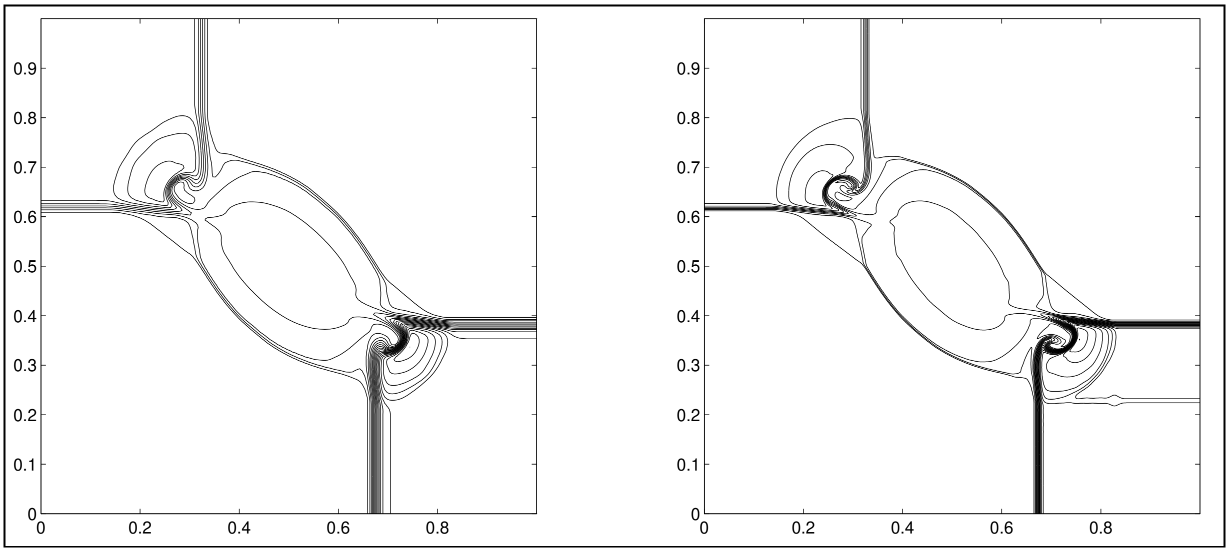

Figure 4.9: Two dimensional Riemann Problem. Solution at time $T = 0.23$ for the initial data reported in Fig. 4.8. Comparison with two different grids. On the left the grid is 200×200; on the right the grid is 400×400.

Lax and Liu in [16] are only second order accurate, we believe that our results are quite striking. In fact, while the positive scheme makes use of the Jacobian and the matrix of eigenvectors of the system of gas dynamics, our scheme requires only the definition of the fluxes. Still, the physics of the problem, apparently, is perfectly caught.

We remark here that suitably tailored upwinding schemes give better resolution that central schemes on specific problems. For example they are able to better resolve contact discontinuities. The main advantage of the central approach is in its simplicity and robustness.

We end our discussion showing the results obtained for Configuration 16 of [16]. The initial condition can be found in Fig. 4.10. The resulting solution is composed of two contact discontinuities, a rarefaction and a shock wave and is shown in Fig. 4.11. We show the results for the density at $T = 0.2$ on a 400×400 grid in Fig. 4.12. The CFL number is $\lambda = 0.5 * 0.2494$. These results should be compared with the corresponding ones in [16], Fig. 16. We note that the shock is sharp, and the resolution of the two contact discontinuities is also good. Moreover, there are no spurious oscillations even though the wave pattern is complex.

5 Conclusions

We have presented the first two-dimensional fourth-order central scheme for the integration of two dimensional systems of conservation laws. First, we would like to comment that this scheme can be easily generalized to 3D problems.

The main feature of the present scheme is its black-box formulation. Although the tests shown are gas dynamics problems, the scheme can be easily applied to other

$\begin{pmatrix}\rho\\u\\v\\p\end{pmatrix}=\begin{pmatrix}1.0222\\-0.6179\\0.1\\1\end{pmatrix}$	$\begin{pmatrix}\rho\\u\\v\\p\end{pmatrix}=\begin{pmatrix}0.5313\\0.1\\0.1\\0.4\end{pmatrix}$
$\begin{pmatrix}\rho\\u\\v\\p\end{pmatrix}=\begin{pmatrix}0.8\\0.1\\0.1\\1\end{pmatrix}$	$\begin{pmatrix}\rho\\u\\v\\p\end{pmatrix}=\begin{pmatrix}1\\0.1\\0.8276\\1\end{pmatrix}$

Figure 4.10: Initial condition for Configuration 16.

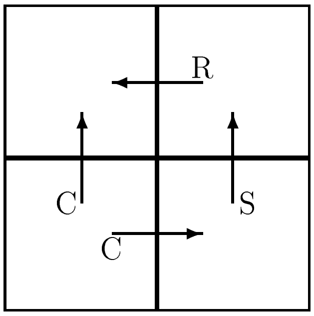

Figure 4.11: Wave structure for Configuration 16. The letters C, R, and S denote contact, rarefaction, and shock waves respectively.

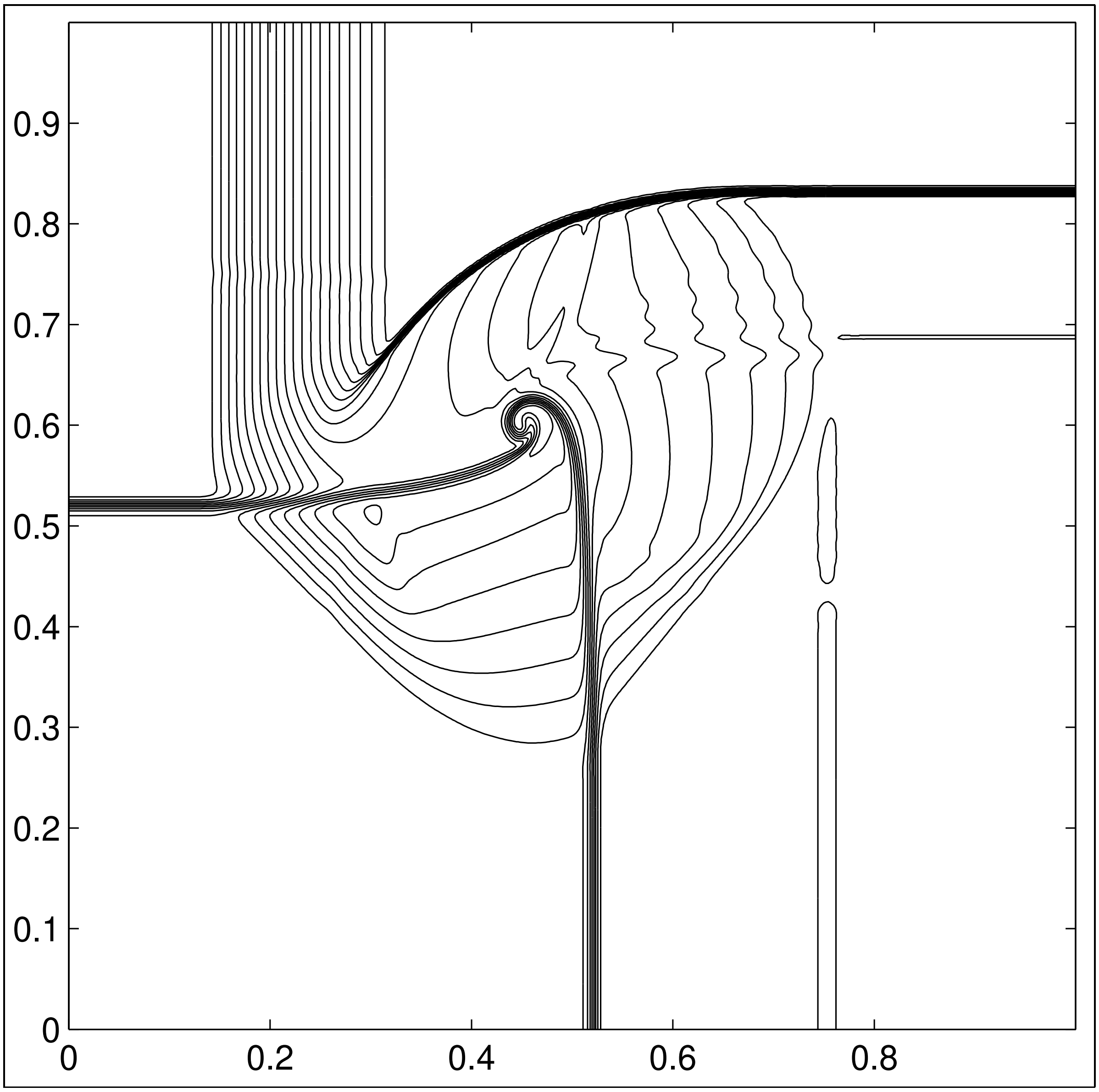

Figure 4.12: Two dimensional Riemann problem. 400×400 grid. Solution at time $T = 0.2$ for the initial data reported in Fig. 4.10.

systems of conservation laws with very small changes in the code. In particular, it is only necessary to supply the flux function and an estimate of the CFL number.

In this perspective, we believe that the fact that we can reproduce the results obtained by the positive scheme of [16] is quite encouraging. The positive scheme in fact requires a detailed knowledge of the structure of the system of conservation laws being integrated, and it is not easily generalized to systems of conservation laws, for which the eigen-structure cannot be written in closed form. Similar results with a semi-discrete central scheme were recently presented in [14].

Naturally, there is still work to do before our scheme can be easily applied to problems of practical interest. Here we list the following:

- The CFL stability restriction of Nessyahu-Tadmor central scheme is $\lambda \leq 1/2$. This value ensures that the solution remains smooth on the edges of the computational cell. Our tests show however that this condition is not sufficient. We believe that a value of $\lambda \leq 0.25$ is a safe estimate. Note that in our study of linear stability [4] for the Central ENO scheme, we found for the fourth order C-ENO one dimensional scheme a stability restriction $\lambda < 2/7 \simeq 0.285$. It may be that the present scheme is stable under a similar restriction. However, in some problems, a less restrictive stability condition seems to be sufficient. Therefore in sections 4.1 and 4.2 we used a larger value of λ. In applications in which the value of λ cannot be tuned to the computation, it is safer to use $\lambda \leq 0.25$ instead. Further work is certainly needed to clarify this issue.

- The issue of boundary conditions needs also to be addressed. A possibility is to introduce a layer of cells close to the boundary on which the conservation laws are integrated with a scheme based on a compact stencil, thereby furnishing all the boundary data needed by the Central WENO scheme.

References

[1] Anile, A. M., Romano, V., Russo, G., *Extended hydrodynamical model of carrier transport in semiconductors*, SIAM J. Appl. Math. **61** (2000), pp.74–101.

[2] Arminjon P., Stanescu D., Viallon M.-C., *A Two-Dimensional Finite Volume Extension of the Lax-Friedrichs and Nessyahu-Tadmor Schemes for Compressible Flow*, Proc. 6th. Int. Symp. on CFD, Lake Tahoe, 1995, M. Hafez and K. Oshima, editors, Vol. IV, pp.7–14.

[3] Bianco F., Puppo G., Russo G., *High Order Central Schemes for Hyperbolic Systems of Conservation Laws*, SIAM J. Sci. Comp., **21**, (1999), pp.294–322.

[4] Bianco F., Puppo G., Russo G., *High Order Central Schemes for Hyperbolic Systems of Conservation Laws*, Int. Series of Num. Math., Vol. 129, Birkhäuser Verlag, 1999.

[5] Friedrichs K. O., Lax P. D., *Systems of Conservation Equations with a Convex Extension*, Proc. Nat. Acad. Sci., **68**, (1971), pp.1686–1688.

[6] Godlewski E., Raviart P.-A., *Numerical Approximation of Hyperbolic Systems of Conservation Laws*, Springer, New York, 1996.

[7] Harten A., Engquist B., Osher S., Chakravarthy S., *Uniformly High Order Accurate Essentially Non-oscillatory Schemes III*, J. Comput. Phys., **71**, (1987), pp.231–303.

[8] Jiang G.-S., Shu C.-W., *Efficient Implementation of Weighted ENO Schemes*, J. Comput. Phys., **126**, (1996), pp.202–228.

[9] Jiang G.-S., Tadmor E., *Nonoscillatory Central Schemes for Multidimensional Hyperbolic Conservation Laws*, SIAM J. Sci. Comp., **19**, (1998), pp.1892–1917.

[10] Kurganov A., Levy D., *A Third-Order Semi-Discrete Scheme for Conservation Laws and Convection-Diffusion Equations*, SIAM J. Sci. Comp., **22**, (2000), pp.1461–1488.

[11] Kurganov A., Noelle S., Petrova G. *semi-discrete central-upwind schemes for hyperbolic conservation laws and Hamilton-Jacobi equations*, SIAM J. Sci. Comp., **23**, (2001), pp.707–740.

[12] Kurganov A., Petrova G., *A Third-Order Semi-Discrete Genuinely Multidimensional Central Scheme for Hyperbolic Conservation Laws and Related Problems*, Numer. Math., **88**, (2001), pp.683–729.

[13] Kurganov A., Tadmor E., *New High-Resolution Central Schemes for Nonlinear Conservation Laws and Convection-Diffusion Equations*, J. Comput. Phys., **160** (2000), pp.214–282.

[14] Kurganov A., Tadmor E., *Solution of Two-Dimensional Riemann Problems for Gas Dynamics without Riemann Problem Solvers*, UCLA CAM-Report 00-34, 2000.

[15] Lax P. D., *Weak Solutions of Non-Linear Hyperbolic Equations and Their Numerical Computation*, CPAM, **7**, (1954), pp.159–193.

[16] Lax P.D., Liu X.D. *Solutions of Two-Dimensional Riemann Problems of Gas Dynamics by Positive Schemes*, SIAM J.Sci.Comp., **19**, No.2, (1998), pp.319–340.

[17] van Leer B., *Towards the Ultimate Conservative Difference Scheme, V. A Second-Order Sequel to Godunov's Method*, J. Comput. Phys., **32**, (1979), pp.101–136.

[18] Levy D., *A Third-order 2D Central Schemes for Conservation Laws*, INRIA School on Hyperbolic Systems, Vol. I (1998), pp.489–504.

[19] Levy D., Puppo G., Russo G., *Central WENO Schemes for Hyperbolic Systems of Conservation Laws*, Math. Model. and Numer. Anal., **33**, no. 3 (1999), pp.547–571.

[20] Levy D., Puppo G., Russo G., *On the Behavior of the Total Variation in CWENO Methods for Conservation Laws*, Appl. Num. Math., **33**, (2000), pp.415–421.

[21] Levy D., Puppo G., Russo G., *A Third Order Central WENO Scheme for 2D Conservation Laws*, Appl. Nume. Math., **33**, (2000), pp.407–414.

[22] Levy D., Puppo G., Russo G., *Compact Central WENO Schemes for Multidimensional Conservation Laws*, SIAM J. Sci. Comp., **22**, (2000), pp.656–672.

[23] Lie K.A., Noelle S., *An Improved Quadrature Rule for the Flux-Computation in High-Resolution Non-Oscillatory Central Difference Schemes for Systems of Conservation Laws in Multidimensions*, preprint.

[24] Liotta S. F., Romano V., Russo G., *Central schemes for balance laws of relaxation type*, SIAM J. Numer. Anal. **38**, (2000), no.4 pp.1337–1356.

[25] Liu X.-D., Osher S., *Nonoscillatory High Order Accurate Self-Similar Maximum Principle Satisfying Shock Capturing Schemes I*, SIAM J. Numer. Anal., **33**, no. 2 (1996), pp.760–779.

[26] Liu X.-D., Osher S., Chan T., *Weighted Essentially Non-oscillatory Schemes*, J. Comput. Phys., **115**, (1994), pp.200–212.

[27] Liu X.-D., Tadmor E., *Third Order Nonoscillatory Central Scheme for Hyperbolic Conservation Laws*, Numer. Math., **79**, (1998), pp.397–425.

[28] Nessyahu H., Tadmor E., *Non-oscillatory Central Differencing for Hyperbolic Conservation Laws*, J. Comput. Phys., **87**, no. 2 (1990), pp.408–463.

[29] Romano V., Russo G., *Numerical solution for hydrodynamical models of semiconductors*, Math. Models Methods Appl. Sci. **10** (2000), pp.1099–1120.

[30] Sanders R., Weiser A., *A High Resolution Staggered Mesh Approach for Nonlinear Hyperbolic Systems of Conservation Laws*, J. Comput. Phys., **1010**, (1992), pp.314–329.

[31] Shu C.-W., *Essentially Non-Oscillatory and Weighted Essentially Non-Oscillatory Schemes for Hyperbolic Conservation Laws* in Advanced Numerical Approximation of Nonlinear Hyperbolic Equations, Lecture Notes in Mathematics (editor: A. Quarteroni), Springer, Berlin, 1998.

[32] Shu C.-W., Osher S., *Efficient Implementation of Essentially Non-Oscillatory Shock-Capturing Schemes, II*, J. Comput. Phys., **83**, (1989), pp.32–78.

[33] Schulz-Rinne C.W., *Classification of the Riemann Problem for Two-Dimensional Gas Dynamics*, SIAM J. Math. Anal., **24**, (1993), pp.76–88.

[34] Schulz-Rinne C.W., Collins J.P., Glaz H.M., *Numerical Solution of the Riemann Problem for Two-Dimensional Gas Dynamics*, SIAM J. Sci. Comp., **14**, (1993), pp.1394–1414.

[35] Sod G., *A Survey of Several Finite Difference Methods for Systems of Nonlinear Hyperbolic Conservation Laws*, J. Comput. Phys., **22**, (1978), pp.1–31.

[36] Stiriba Y., Marquina A., Donat R., *Equilibrium Real Gas Computations using Marquina's Scheme*, preprint, 2000.

[37] Tadmor E., *Approximate Solutions of Nonlinear Conservation Laws*, in Advanced Numerical Approximation of Nonlinear Hyperbolic Equations, Lecture Notes in Mathematics (editor: A. Quarteroni), Springer, Berlin, 1998.

[38] Woodward P., Colella P., *The Numerical Simulation of Two-Dimensional Fluid Flow with Strong Shocks*, J. Comput. Phys., **54**, (1984), pp.115–173.

[39] Zennaro M., *Natural Continuous Extensions of Runge-Kutta Methods*, Math. Comp., **46**, (1986), pp.119–133.